Mineralogical Magazine (2022), **86**, 586–605
doi:10.1180/mgm.2022.7

CAMBRIDGE UNIVERSITY PRESS

Article

Special Issue dedicated to Peter Williams

Hellandite-(Y)–hingganite-(Y)–fluorapatite retrograde coronae: a novel type of fluid-induced dissolution–reprecipitation breakdown of xenotime-(Y) in the metagranites of Fabova Hoľa, Western Carpathians, Slovakia

Martin Ondrejka[1]*, Alexandra Molnárová[1], Marián Putiš[1], Peter Bačík[1], Pavel Uher[1], Bronislava Voleková[2], Stanislava Milovská[3], Tomáš Mikuš[3] and Libor Pukančík[4]

[1]Department of Mineralogy, Petrology and Economic Geology, Faculty of Natural Sciences, Comenius University, Ilkovičova 6, Mlynská dolina, 842 15, Bratislava, Slovakia; [2]Slovak National Museum, Natural History Museum, Vajanského nábrežie 2, P.O. BOX 13, 810 06 Bratislava, Slovakia; [3]Earth Science Institute of the Slovak Academy of Sciences, Ďumbierska 1, 974 01, Banská Bystrica, Slovakia; and [4]HBP (Inc.), Mining Facility Čáry, Matice slovenskej 10, 971 01 Prievidza, Slovakia

Abstract

Two contrasting reaction coronae were developed around rare earth element (REE) accessory phosphates in Variscan metagranitic rocks, which have been overprinted by Alpine blastomylonitisation from the Fabova Hoľa Massif, in the Veporic Unit, Western Carpathians, Central Slovakia. The Th–U–Pb total EPMA age determination of primary magmatic monazite-(Ce) from the metagranite indicates a Carboniferous (Mississippian, Tournaisian) age of 355 ± 1.9 Ma. Monazite-(Ce) breakdown resulted in impressive, though common, fluorapatite ± Th-silicate + allanite-(Ce) + clinozoisite coronae. The alteration of xenotime-(Y) produced a novel type of secondary coronal micro-texture consisting of a massive fluorapatite mantle zone and tiny satellite crystals of hellandite-(Y) [$(Ca,REE)_4Y_2Al\square_2(B_4Si_4O_{22})(OH)_2$] and hingganite-(Y) [$Y_2\square Be_2Si_2O_8(OH)_2$] of ~1–5 μm, and rarely ≤10 μm in size. The localised occurrence of Y–B–Be silicates, which are associated closely with other secondary minerals, suggests the involvement of B and Be during the metasomatic alteration transformation of xenotime-(Y). General reactions for monazite-(Ce) and xenotime-(Y) decomposition, including the fluids involved, can be written as follows: Mnz + (Ca, Fe, Si, Al and F)-rich fluid → FAp + Ht + Aln + Czo; Xtm + (Ca, Fe, Si, Al, F, B and Be)-rich fluid → FAp + Hld + Hin + Czo.

The granitic rocks underwent Early Cretaceous burial metamorphism under greenschist- to lower amphibolite-facies *P–T* conditions. Subsequently, Alpine post-collisional uplift and exhumation of the Veporic Unit, starting from the Late Cretaceous epoch, was accompanied by a retrograde tectono-metamorphic overprint; the activity of external fluids, caused the formation of secondary coronae minerals around monazite-(Ce) and xenotime-(Y). A portion of B (± Be) should have been liberated from the metagranite feldspars, micas, or xenotime-(Y) enriched in $(Nb,Ta)BO_4$ (schiavinatoite or béhierite) components. However, the principal source of B and Be in fluids necessary for the production of hellandite and hingganite, was probably of external origin from adjacent magmatic, metamorphic, or sedimentary rocks (Permian granites, rhyolites and sedimentary rocks, and Palaeozoic metapelites).

Keywords: hellandite-(Y), hingganite-(Y), Y–B–Be silicate, xenotime-(Y), dissolution–reprecipitation, reaction coronae, metagranite, Fabova Hoľa, Western Carpathians, Slovakia

(Received 23 August 2021; accepted 13 January 2022; Accepted Manuscript published online: 24 January 2022; Associate Editor: Aniket Chakrabarty)

Introduction

Together with allanite-(Ce), monazite-(Ce) and xenotime-(Y) are the most important carriers of rare earth elements (REE) in common magmatic rocks and metamorphic rocks with granitic and metapelitic protoliths (e.g. Bea, 1996; Förster, 1998a, 1998b; Spear and Pyle, 2002; Gieré and Sorensen, 2004). A detailed study of their composition, stability and breakdown processes provides us with an understanding of REE relationships and processes that occur during petrogenesis and evolution of the

*Author for correspondence: Martin Ondrejka, Email: martin.ondrejka@uniba.sk
This paper is part of a thematic set that honours the contributions of Peter Williams.
Cite this article: Ondrejka M., Molnárová A., Putiš M., Bačík P., Uher P., Voleková B., Milovská S., Mikuš T. and Pukančík L. (2022) Hellandite-(Y)–hingganite-(Y)–fluorapatite retrograde coronae: a novel type of fluid-induced dissolution–reprecipitation breakdown of xenotime-(Y) in the metagranites of Fabova Hoľa, Western Carpathians, Slovakia. *Mineralogical Magazine* **86**, 586–605. https://doi.org/10.1180/mgm.2022.7

parental rock (Wark and Miller, 1993; Bea, 1996; Gratz and Heinrich, 1997; Heinrich *et al.*, 1997; Förster, 1998a, 1998b; Poitrasson *et al.*, 2002; Pyle *et al.*, 2001; Spear and Pyle, 2002; Wing *et al.*, 2003; Kohn and Malloy, 2004; Ondrejka *et al.*, 2012, 2016; Berger *et al.*, 2008; Janots *et al.*, 2008; Uher *et al.*, 2009, 2015; Harlov *et al.*, 2011 and references therein). In addition, monazite-(Ce) and xenotime-(Y) are essential for petrochronology (e.g. Parrish, 1990; Montel *et al.*, 1996; Williams *et al.*, 2007; Engi, 2017).

Although these minerals commonly crystallise as primary magmatic or metamorphic accessory phases, younger post-magmatic or metamorphic hydrothermal fluids can cause their partial-to-complete transformation to low-grade neoblasts. For example, the commonly observed breakdown of monazite-(Ce) includes a subsolidus retrograde corona around its partly dissolved core with distinctive concentric mineral zones of apatite ± Th-silicate/oxide, and allanite-(Ce) to REE-rich epidote or clinozoisite (e.g. Broska and Siman, 1998; Finger *et al.*, 1998, 2016; Budzyń *et al.*, 2010; Ondrejka *et al.*, 2012, 2016; Upadhyay and Pruseth, 2012; Lo Pò *et al.*, 2016; Ji *et al.*, 2021). This microtexture is documented mostly in low- to medium-temperature metagranitoids with primary magmatic monazite-(Ce). However, it can also occur in metapelites if the high-temperature metamorphic monazite-(Ce) destabilises during post-peak metamorphic evolution (Majka and Budzyń, 2006; Finger *et al.*, 2016; Lo Pò *et al.*, 2016). Similar reaction coronae around xenotime-(Y) in granitoids and metapelites (Broska *et al.*, 2005; Majka and Budzyń, 2006; Janots *et al.*, 2008; Majka *et al.*, 2011; Broska and Petrík, 2015; Budzyń *et al.*, 2018; Hentschel *et al.*, 2020), or the partial compositional alteration of xenotime-(Y) via dissolution–reprecipitation resulting in a texture characterised by thorite ($ThSiO_4$) and uraninite (UO_2) inclusions (Hetherington and Harlov, 2008; Ondrejka *et al.*, 2016), are less frequent. Experiments suggest the significant dissolution, etching, and alteration of monazite-(Ce) and xenotime-(Y) by common metamorphic and igneous fluids, and the formation of porous textures and various secondary phases, are dependent on the *P*–*T*–*X* conditions (Hetherington *et al.*, 2010; Harlov *et al.*, 2011; Harlov and Wirth, 2012; Budzyń *et al.*, 2011, 2017), as well as on the presence of low-*T* metamorphic or post-magmatic-hydrothermal fluids in granitic systems (Budzyń and Kozub-Budzyń, 2015).

In this investigation, partially-decomposed primary magmatic monazite-(Ce) and xenotime-(Y) in mylonitised metagranites from the Variscan basement of the Fabova Hoľa granitic complex in the Veporic Unit, Central Slovakia are reported and interpreted (Fig. 1). Whereas retrograde destabilisation of monazite-(Ce) and remobilisation of light rare earth elements (LREE) results in an impressive corona of fluorapatite ± Th-silicate–allanite-(Ce)–clinozoisite, decomposition of xenotime-(Y) results in a novel type of reaction corona, including fluorapatite, hellandite-(Y) and hingganite-(Y) mineral zones, involving heavy rare earth elements (HREE) + Y, and also B and Be mobility. In this investigation, textural and compositional data, X-ray mapping, Th–U–total Pb age determination of monazite-(Ce) and Raman spectra all contribute to understanding the stability and breakdown products of REE, B and Be accessory minerals, their evolution, and behaviour during fluid-driven processes. Consequently, we describe a possible scenario regarding their origin and fluid sources responsible for their alteration. Moreover, the unusual Y–B–Be silicate reaction corona minerals, hellandite and hingganite, around xenotime-(Y) are documented for the first time.

Geological setting

Regional geology

The Variscan basement structure of the Western Carpathians is composed of several structural units that are recognisable, even though there has been Alpine, mainly Cretaceous, tectono-metamorphic overprinting (Putiš, 1992). The Alpine structure of the Inner Western Carpathians is related to the evolution of the Cretaceous collisional wedge. The south–north progradation of this wedge has been dated between ca. 130 and 50 Ma according to ^{40}Ar–^{39}Ar radiometric age determination of phengitic white mica and muscovite from the thrust-fault shear zones (Putiš *et al.*, 2009b).

The REE accessory minerals investigated occur in mylonitised granites of the Variscan basement, which are included in the Late Cretaceous Veporic Unit of the Inner Western Carpathians (e.g. Plašienka *et al.*, 1997). Calc-alkaline tonalites to granites of I/S-type affinity intruded into the Early Palaeozoic crystalline basement complex of paragneisses, granitic orthogneisses, amphibolites, rare eclogites, calc-silicate marbles and migmatites of the Upper Variscan structural Unit or the Tatra Nappe (Putiš 1992; Bezák 1994; Putiš *et al.*, 2003, 2008, 2009b; Janák *et al.*, 2007). Recent *in situ* U–Pb radiometric age determination in zircon indicates that their meso-Variscan, Upper Devonian to Carboniferous age interval of emplacement was ~365–350 Ma (Gaab *et al.*, 2005; Broska *et al.*, 2013; Kohút and Larionov 2021).

Granitic rocks also occur in the form of individual small intrusions crosscutting the basement rocks (Ondrejka *et al.*, 2021 and references therein). Similarly, dykes of Permian acidic-to-basic volcanic rocks, together with microgranites, intruded the crystalline basement rocks, or occur as intercalations within the Permian sedimentary successions (Kotov *et al.*, 1996; Vozárová *et al.*, 2016). These are covered by Triassic metaquartzites, marbles and calc-schists of the sedimentary cover (Foederata Group) of the Veporic Unit crystalline basement (Plašienka *et al.*, 1997).

Intrusions and lava flows of Miocene calc-alkaline diorites and andesites (~12 Ma; Konečný *et al.*, 2015a, 2015b) belong to the youngest Neo-Alpine magmatic event in the part of the Veporic Unit studied. They also intruded the Variscan granitic rocks of the Fabova Hoľa Massif. These plutonic and volcanic rocks originated as a consequence of subduction of the Outer Western Carpathian basement underneath the Inner Western Carpathians (Pécskay *et al.*, 2006; Lexa *et al.*, 2010).

Petrographic characterisation of the metagranitic rocks

The Veporic crystalline basement south of the Late Cretaceous Pohorelá tectonic line consists mostly of metagranitoids (tonalites, granodiorites and porphyric-to-homogeneous granites) of the meso-Variscan Vepor pluton (Kohút *et al.*, 2008). Relics of magmatic minerals, such as quartz, plagioclase, K-feldspar, biotite, muscovite, fluorapatite, zircon and REE accessory minerals occur in the newly formed or recrystallised mineral assemblage of quartz, albite, Ti-poor biotite, celadonite-rich muscovite ('phengite'), chlorite, epidote, clinozoisite, calcite, titanite, rutile, and several tiny euhedral garnets that define the mylonitic foliation (Putiš, 1994). The lineation of the mylonitic foliation is defined by newly formed biotite, chlorite, and sericitic phengite in a roughly E–W (to WNW–ESE) direction. There are common transitions from granitic and tonalitic protomylonites to augen granite–gneisses (mylonites) and phyllonites (blastomylonites). These micro-structures indicate the ductile behaviour of quartz

https://doi.org/10.1180/mgm.2022.7 Published online by Cambridge University Press

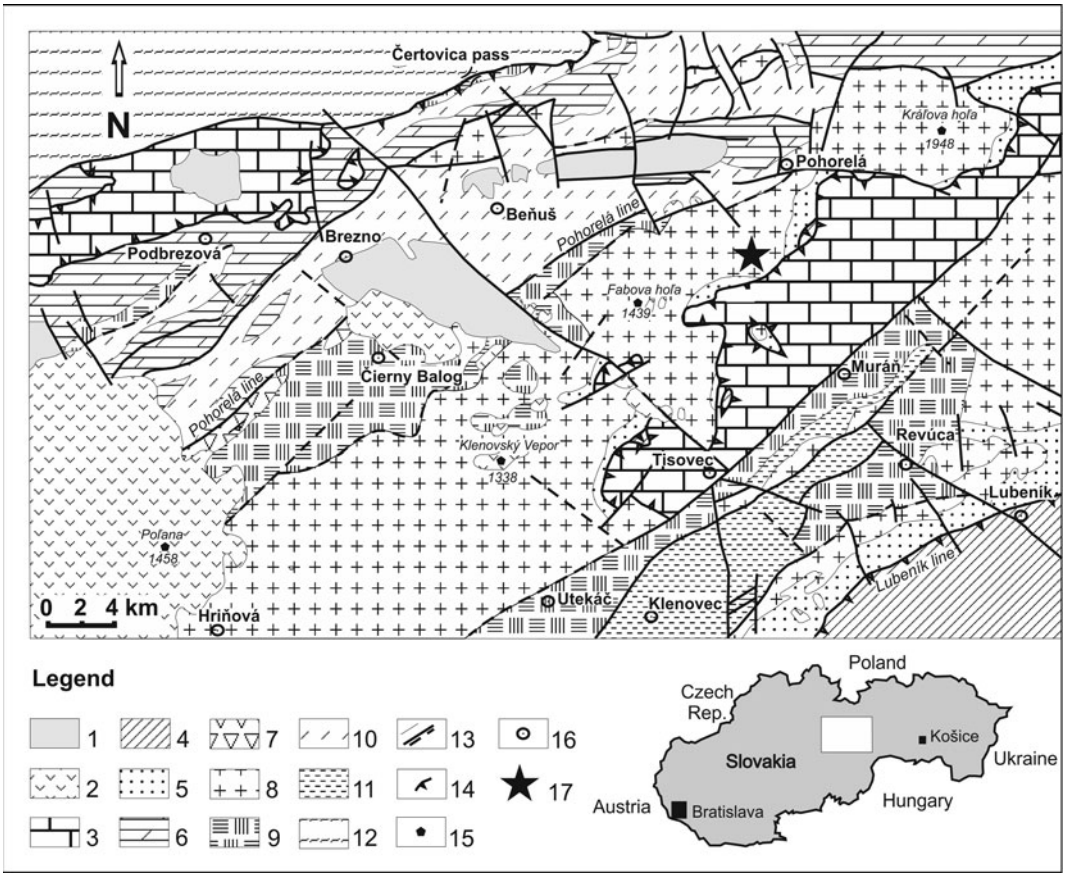

Fig. 1. Geology of the Veporic Unit of the Central Western Carpathians (modified from Ondrejka *et al.*, 2016). Compiled on the basis of the 1:500,000 scale geological map of Slovakia (Biely *et al.*, 1996). Subdivision of tectonic units from top to bottom: 1 – Upper Cretaceous, Palaeogene, Neogene and Quaternary sedimentary rocks, undivided (post-tectonic cover); 2 – Neogene volcanic and volcanoclastic rocks; 3 – Permian to Mesozoic sedimentary rocks undivided, in nappe position; 4 – Early to Late Palaeozoic – low-grade, metamorphosed sedimentary and volcanic rocks (Gemeric basement-cover complex, undivided; Lower Variscan Unit); 5 – Late Palaeozoic to Mesozoic para-autochthonous low-grade metamorphosed sedimentary and volcanic rocks of the South Veporic cover (Revúca Group, Foederata Unit); 6 – Permian to Mesozoic subautochthonous anchi- to low-grade, metamorphosed sedimentary and volcanic rocks of the North Veporic cover; 7 – Permian porphyric granites of the Hrončok type; 8 – Variscan granites, granodiorites and tonalites; 9 – gneisses to migmatites, orthogneisses, amphibolites, layered amphibolites, metagabbros, eclogites, metaperidotites, microgranites, pegmatites and aplites (Upper Variscan Unit); 10 – mica schists to gneisses, rare amphibolites (Middle Variscan Unit); 11 – phyllites, mica schists, greenschists to amphibolites, metasandstones, metavolcanics and metacarbonates (Lower Variscan Unit); 12 – Tatric basement-cover complex, undivided (Upper Variscan Unit); 13 – geological boundaries and faults: proved or assumed; 14 – nappe boundaries; 15 – ground elevation; 16 – town or city; and 17 – Fabova Hoľa metagranite (FAH-3 sample).

and the semi-ductile behaviour of feldspars in the mylonites. They reflect mostly the last top-to-the E(ESE) extensional deformation along the ductile low-angle normal faults in the basement and cover rocks during post-metamorphic exhumation (Putiš, 1994). The mylonitisation processes had an isochemical-to-allochemical character with increasing deformation in two different stages. The first stage of deformation, which was the transition from protomylonite to mylonite, usually is of an isochemical character, with restricted chemical changes. During the second stage, which was the transition from mylonite to ultramylonite/blastomylonite, local deformation occurred with the loss of Ca and Na and the gain of K, Mg (± Fe) in the mylonite/blastomylonite due to higher ductile strain localisation and increased fluid activity. The most immobile elements appear to be Si, Ti and Al (Putiš *et al.*, 1997a). The basement mylonites reflect deformational conditions of ~400–500°C at depths of 20–25 km (Putiš, 1994; Putiš *et al.*, 1997a, 1997b). The exhumation age of the granitoid rocks has been determined from the newly formed phengite at ~100–85 Ma (Maluski *et al.*, 1993; Dallmeyer *et al.*, 1993, 1996; Putiš *et al.*, 2009b). Post-collisional exhumation is constrained by zircon fission tracks with ages of 88 to 62 Ma from the Veporic tectonic units (Plašienka *et al.*, 2007; Vojtko *et al.*, 2016). The apatite fission track ages of 63–55 Ma and apatite (U–Th)/He ages of 62–31 Ma from the southern Veporic Unit (Vojtko *et al.*, 2016) suggest the upper crustal level of the exhumation and cooling to temperatures below ca. 250°C (zircon fission tracks), 125°C (apatite fission tracks) or to ca. 70°C [apatite (U–Th)/He], respectively.

Analytical methods

The minerals were sampled from natural outcrops and investigated in polished thin sections of metagranites (15 rock samples). The petrography of the samples was investigated using a polarised optical microscope.

The composition of the minerals was determined by electron probe microanalysis (EPMA) in wavelength-dispersive spectrometry (WDS) mode and X-ray elemental mapping, using a JEOL JXA–8530 F field emission electron microprobe at the Earth Science Institute of the Slovak Academy of Sciences in Banská Bystrica, Slovakia. An accelerating voltage of 15 kV and a

https://doi.org/10.1180/mgm.2022.7 Published online by Cambridge University Press

beam current of 40–20 nA was used with other relevant analytical conditions chosen according to the mineral type. The typical spot beam diameter varied from 2 to 8 μm; a more focused ≤1–3 μm beam was used for some Y–B–Be silicates, and occasionally for secondary and heterogeneous fluorapatite. The EPMA was calibrated using natural and synthetic standards (Supplementary table S1), and raw counts were converted to wt.% of oxides using a full *ZAF* matrix correction. Corrections of line interferences for Nd→Ce, Eu→Nd, Eu→Pr, Gd→Ho, Tm→Sm, Nd→Ce, Lu→Dy, Lu→Ho, U→Th, K→U and V→Ti followed Åmli and Griffin (1975). Element amounts of <0.01 wt.% are below the detection limit.

Monazite Th–U–total Pb age determination was performed using a CAMECA SX–100 microprobe at the Department of Electron Microanalysis at the State Geological Institute of Dionýz Štúr in Bratislava. Operating conditions consisted of 15 kV accelerating voltage, 180 nA beam current and a 3 μm beam diameter. The PAP matrix correction factors were used (Supplementary table S1). Analytical lines free of overlap were selected preferentially. Mutual interferences among the REE were corrected using empirical correction factors. The Pb*Mα* line is overlapped by La*Lα*, Th*Mζ*1, Th*Mζ*2 and Y*Lγ*2,3 lines. The weak interference by the La*Lα* line was ignored. The U*Mß* line is overlapped by Th*Mζ*, Th*M*3-*N*4 and Th*M*5-*P*3 lines. Pb*Mα* line overlaps were resolved with a curved exponential background. Monazite age determination included the measurement of 7–9 monazite age standards, as well as the application of correction dependencies derived from the measured compositions. Further details and description of the age determination procedure (MARC) can be found in Konečný *et al.* (2018).

Raman analysis was performed with a Horiba Jobin-Yvon LabRAM-HR 800 spectrometer in the Earth Science Institute of the Slovak Academy of Sciences, Banská Bystrica, Slovakia. The spectrometer is equipped with a Czerny-Turner monochromator with a 600 gr/mm grating and a Peltier-cooled Synapse CCD detector (Horiba Jobin-Yvon), and is connected to an Olympus BX41 microscope with a long-working distance 100×0.8 objective. The lateral resolution of the system is <2 μm. Samples were irradiated with He–Ne (633 nm) and Nd:YAG (532 nm) lasers. The Rayleigh line and a Teflon standard were used for calibration. The spectra were collected in 10–25 acquisitions that lasted 600 s or 1000 s per spectral window and processed using *LabSpec 5* (Horiba) and *PeakFit1* programs (SeaSolve Software Inc.). The Raman spectra were also obtained using a Thermo Scientific DXR3xi Raman Imaging microscope at the Slovak National Museum – The Natural History Museum in Bratislava, Slovakia. Several lasers were used during the investigation, mainly a 532 nm doubled Nd: YVO_4 DPSS excitation laser and a 633 nm He–Ne laser, 100 × objective, a 25 μm confocal pinhole and an EMCCD detector. Approximately 80 spectra were acquired from the mineral phases investigated at a laser power of 10–20 mW for between 0.5 and 2 s (20 scans for a cycle). The processing of spectra (including fitting by Voigt functions) was carried out using the Thermo Fisher Scientific *OMNIC v. 9.11* software package.

Spectra were collected in the 100–1200 cm^{-1} and 100–4000/6000 cm^{-1} ranges and from approximately the same spots as the EPMA, but shifted slightly from the mark left by the electron beam. This confirmed the composition, and thus distinct Raman bands were obtained. For accurate interpretation of the spectra belonging to hingganite-(Y) [$Y_2\square Be_2Si_2O_8(OH)_2$], macroscopic samples of gadolinite-(Y) [$Y_2Fe^{2+}Be_2Si_2O_8O_2$] from the localities of Tinbo, Sweden and Hitterö, Norway from the collections at the Slovak Natural History Museum, Bratislava were also analysed by Raman spectroscopy.

The multi-element lithogeochemistry of powdered samples was performed by Bureau Veritas (AcmeLabs) in Vancouver, Canada, by X-ray fluorescence (XRF) for major elements, and inductively-coupled plasma atomic emission spectrometry (ICP–AES), together with inductively-coupled plasma mass spectrometry (ICP–MS) for the trace and rare earth elements.

Element contents in the mineral formulae are expressed in atoms per formula unit (apfu). The hellandite formulae (redefined by Oberti *et al.*, 2019) were normalised on the basis of $Si^{4+} + P^{5+} = 4$ cations and the partition of total manganese between Mn^{2+} (*Y* site) and Mn^{3+} (*Z* site) was calculated from ideal stoichiometry and neutral charge balance. Gadolinite-group nomenclature and mineral formulae calculation (Bačík *et al.*, 2017) were used. The hingganite-(Y) formulae were normalised on the basis of *A* = 2 cations, the OH^- content was calculated as $(2^{*M}\square)$ – F, where $^M\square$ is a vacancy at the *M* site. The B_2O_3 and BeO contents (wt.%) were calculated from the charge balance according to Be = 6 – [20 – Σ*PC* – OH^-] (where *PC* is the sum of charges for all cations except B and Be) and B = 2 – Be. The formulae of epidote-group minerals were normalised on the basis of Σ(*A* + *M* + *T*) = 8 cations following the procedure of Armbruster *et al.* (2006), the partition of total Fe between Fe^{2+} and Fe^{3+} was calculated from ideal stoichiometry and neutral charge balance, and the H_2O content was calculated assuming $OH^- + F^- + Cl^- = 1$ apfu. Fluorapatite was calculated on the basis of Σ(*M* + *T*) = 8 cations and $OH^- + F^- + Cl^- = 1$ apfu (Pasero *et al.*, 2010). Monazite-(Ce) and xenotime-(Y) formulae were normalised to 4 oxygen atoms.

Sample description and accessory mineral assemblage

We investigated 15 polished thin sections of mylonitised metagranitic rocks from the Fabova Hoľa Massif Vepor pluton, in the Slovak Ore Mountains (Veporic Unit). They usually contain accessory monazite-(Ce) with secondary reaction coronae of fluorapatite + allanite-(Ce) to epidote or clinozoisite. However, sample FAH-3 also contains accessory xenotime-(Y) with different, newly described fluorapatite + hellandite-(Y) + hingganite-(Y) reaction coronae. This sample is described in detail. FAH-3 was collected from a small, natural outcrop in the Hronec valley, ~500 m south from the Klátna gamekeeper's lodge on the western slope of Klátny Grúň hill, (48°47′41″N 19°56′26″E).

The rock studied (FAH-3) represents a foliated blastomylonitised porphyric metagranite. The texture is grano-lepidoblastic to lepidoblastic with blastomylonitic foliation. The primary magmatic minerals include quartz-1, plagioclase, K-feldspar, biotite-1 and muscovite-1, with accessory zircon, fluorapatite, monazite-(Ce), xenotime-(Y) and Fe–Ti oxides (ilmenite>magnetite). In addition, FAH-3 contains a newly-formed and recrystallised mineral assemblage, which includes quartz-2, albite, phengitic muscovite, epidote to clinozoisite, Ti-depleted biotite-2 and muscovite-2.

Quartz-1 forms anhedral crystals with distinct undulatory extinction and is rimmed by fine-grained aggregates of recrystallised quartz-2. Subhedral plagioclase (oligoclase with An_{20-15}) is replaced extensively by fine-crystalline white mica aggregates (sericitisation) and irregular rim zones of secondary albite (~An_{01}). White-to-grey K-feldspar (98 mol.% orthoclase/microcline, 2 mol.% albite, 1 mol.% celsian on average) forms large euhedral phenocrysts (up to 4 cm in size) locally, with Carlsbad twinning and inclusions of plagioclase and biotite-1. Biotite-1 has an annite-dominant composition [Fe/(Fe + Mg) = 0.55–0.57;

https://doi.org/10.1180/mgm.2022.7 Published online by Cambridge University Press

^{T}Al = 1.17–1.24 apfu] and forms subhedral, distinctly foliated crystals, locally baueritised to muscovite-2, or chloritised with tiny sagenitic inclusions of titanite and rutile. The existence of primary magmatic muscovite-1 is possible, however it was not clearly proved by optical or microprobe study. Muscovite-2 occurs as very fine-grained aggregates ('sericite') or subhedral to euhedral platy crystals (up to 0.3 mm in size), usually with phengitic (celadonite-rich muscovite) composition (3.1–3.3 apfu Si; Fe + Mg = 0.4–0.6 apfu). The representative assemblage of primary and secondary rock-forming minerals is shown in Fig. 2*a*.

Primary fluorapatite (apatite-1) and zircon are the dominant accessory phases. Apatite-1 forms large, scattered euhedral-to-subhedral crystals up to 300 μm in size and associated with moderately chloritised biotite, quartz, albite and K-feldspar, together with accessory monazite-(Ce), xenotime-(Y) and their breakdown products. Zircon forms large euhedral prismatic crystals up to 300 μm in size (occasionally up to 500 μm), usually in association with apatite-1 and enclosed in biotite-1. Zircon has regular, magmatic oscillatory zoning, rare inherited xenocrystic cores and locally present inclusions of thorite and coffinite.

Representative whole-rock compositions are in Table 1. In general, the granites investigated have high SiO_2 (67–75 wt.%), Al_2O_3 (14–17 wt.%) and $Na_2O + K_2O - CaO$ (4–8 wt.%) values and low, but varying TiO_2 (0.05–0.5 wt.%) and P_2O_5 (0.04–0.2 wt.%) values, together with moderate $FeO_{tot}/(FeO_{tot} + MgO)$ (0.70–0.79). Their A/CNK and A/NK ratios range from 1.0 to 1.2 and 1.2 to 1.6, respectively, corresponding to a peraluminous composition. Trace-element geochemistry shows enrichment in Ba (390 to 1180 ppm) and Sr (230 to 400 ppm), as well as varying REE+Y (50 to 350 ppm) and Y (8 to 20 ppm). The concentration of light elements also shows enrichment, especially in B (~15 to 20 ppm; Marsina *et al.*, 1999) and Be (2 to 4 ppm). In general, they show an S-type or hybrid S/I-type affinity and are characterised by calc-alkaline compositions and low contents of Mg, Ca, Sr, Ba, Zr and REE when compared with I-type granites (cf. Broska and Uher, 2001; Broska *et al.*, 2004).

Minerals of the reaction coronae

Fluorapatite–allanite-(Ce)–clinozoisite corona around monazite-(Ce)

The primary magmatic monazite-(Ce) is a relatively abundant accessory mineral of the FAH-3 metagranite sample. It is distributed equally throughout the host metagranite, and it is usually enclosed in chloritised biotite-1, or albite, with the association of zircon and apatite-1; close overgrowths and intergrowths of primary monazite-(Ce) with apatite-1 are common. The monazite is mostly preserved as partly-dissolved relics up to 200 μm in the centre of the coronae mineral aggregates. The monazite coronae aggregates attain ~100 to 250 μm in size and have well-developed concentric mineral zoning (Fig. 2b–d). The inner corona zone consists of polygonal, secondary fluorapatite (apatite-2a) with minute prismatic $ThSiO_4$ inclusions (≤1 μm), which are most probably huttonite rather than dimorphous thorite. This is concluded from their high Th, Si, and LREE>HREE EDS signals and several WDS analyses of the average composition. More precise WDS analyses of these $ThSiO_4$ inclusions are not possible due to analytical limitations. The outer corona zone comprises acicular to prismatic aggregates of secondary allanite-(Ce) to REE-rich epidote or clinozoisite with diffuse boundaries and radial intergrowth with the host-rock matrix (Fig. 2b–d). The corona has mostly a symmetrical shape (Fig. 2b), consisting sometimes of a lopsided corona, or an asymmetrical coronal tail of allanite-(Ce)–clinozoisite outwards from the monazite-(Ce) as seen in Fig. 2c, or a tiny collar of allanite-(Ce) ± monazite-(Ce) relics that defines the euhedral habit of the former intergrowths of apatite-1 and monazite-(Ce) (Fig. 2d). In some places, apatite-2–allanite-(Ce)–clinozoisite coronae without a monazite-(Ce) core occur, which either represent a different orientation of the non-centred cut in the corona structure or indicate a complete replacement of the monazite-(Ce).

The preserved monazite-(Ce) relics have a relatively homogeneous composition and contain only minor amounts of the cheralite ($Ca_{0.5}Th_{0.5}PO_4$) and huttonite ($ThSiO_4$) components (X_{chrl} ≤10, occasionally ≤20 mol.%; X_{hutt} ≤5 mol.%, Table 2). The chondrite-normalised REE distribution patterns shows a typical LREE>HREE slope ($La_N/Yb_N = 77$) and a distinct Eu negative anomaly (Fig. 3). The relatively high actinide content permits *in situ* Th–U–total Pb EPMA age determination of primary magmatic monazite-(Ce), which gave a Carboniferous (Mississippian, Tournaisian) age of 355 ± 1.9 Ma ($n = 200$, MSWD: 1.68; Fig. 4).

The composition of apatite-2a is relatively uniform and represents an almost pure $Ca_5(PO_4)_3F$ end-member (Table 2). The total REE content is generally low and never exceeds 3.5 wt.% $(REE,Y)_2O_3$ (0.1 apfu REE+Y), thus indicating only a subordinate presence of the fluorbritholite $[(REE,Ca)_5(SiO_4)_3F]$ component. Among REE, it has LREE>HREE+Y (av. $LREE_2O_3 = 1.84$ wt.% vs. av. $HREE,Y_2O_3 = 0.44$ wt.%). The concentrations of actinides (especially Th) rarely reach up to 5.5 wt.% $ThO_2 + UO_2$ (0.11 apfu Th and U), and together with elevated Si content (2.24 wt.% SiO_2, 0.2 apfu Si) suggest the presence of Th-silicate nanoinclusions.

The secondary epidote-group minerals have a large variation in REE + Y + Th (0.02–1.00 apfu) and total Al values (1.57–2.47 apfu), thus indicating that varying amounts of allanite–ferriallanite and clinozoisite–epidote solid-solution components are present (Table 2). In contrast, clinozoisite has Fe^{3+} enrichment in the *M*3 position and a lower Al content, which indicates a significant epidote component. In general, the composition of the epidote-group minerals solid solution is controlled by a dominant $^{A2}REE + {}^{M3}Fe^{2+} \leftrightarrow {}^{A2}Ca + {}^{M3}(Fe, Al)^{3+}$ substitution mechanism.

Fluorapatite–hellandite-(Y)–hingganite-(Y) coronae around xenotime-(Y)

Primary xenotime-(Y) is a relatively scarce, accessory mineral, but, when present, it always occurs as solitary crystals that are >100 μm in size in albite or biotite and surrounded by a secondary reaction corona. The reaction coronae around the primary xenotime-(Y) has an inner zone of typically highly-porous secondary fluorapatite (apatite-2b), which is analogous to the monazite coronae, though differs distinctly in the REE minerals of the outer zone. This novel type of secondary reaction micro-texture consists of Y–B–Be silicate minerals instead of the expected allanite-(Y) and/or HREE+Y-rich epidote. These Y–B–Be phases are represented by hellandite-(Y) $[(Ca,REE)_4Y_2Al\square_2(B_4Si_4O_{22})(OH)_2]$ and hingganite-(Y) $[Y_2\square Be_2Si_2O_8(OH)_2]$. Both minerals occur as numerous tiny anhedral to subhedral satellite crystals and/or chain-like aggregates and intergrowths (usually ~1–5 μm, occasionally ≤10 μm in size) positioned between the apatite-2 and the clinozoisite zone (Fig. 2e–h). The presence of these minerals is also confirmed by X-ray compositional mapping, including B (Fig. 5) and Raman spectra (see section on Raman spectroscopy). A visible disproportion between the massive apatite-2b zone and the thin

https://doi.org/10.1180/mgm.2022.7 Published online by Cambridge University Press

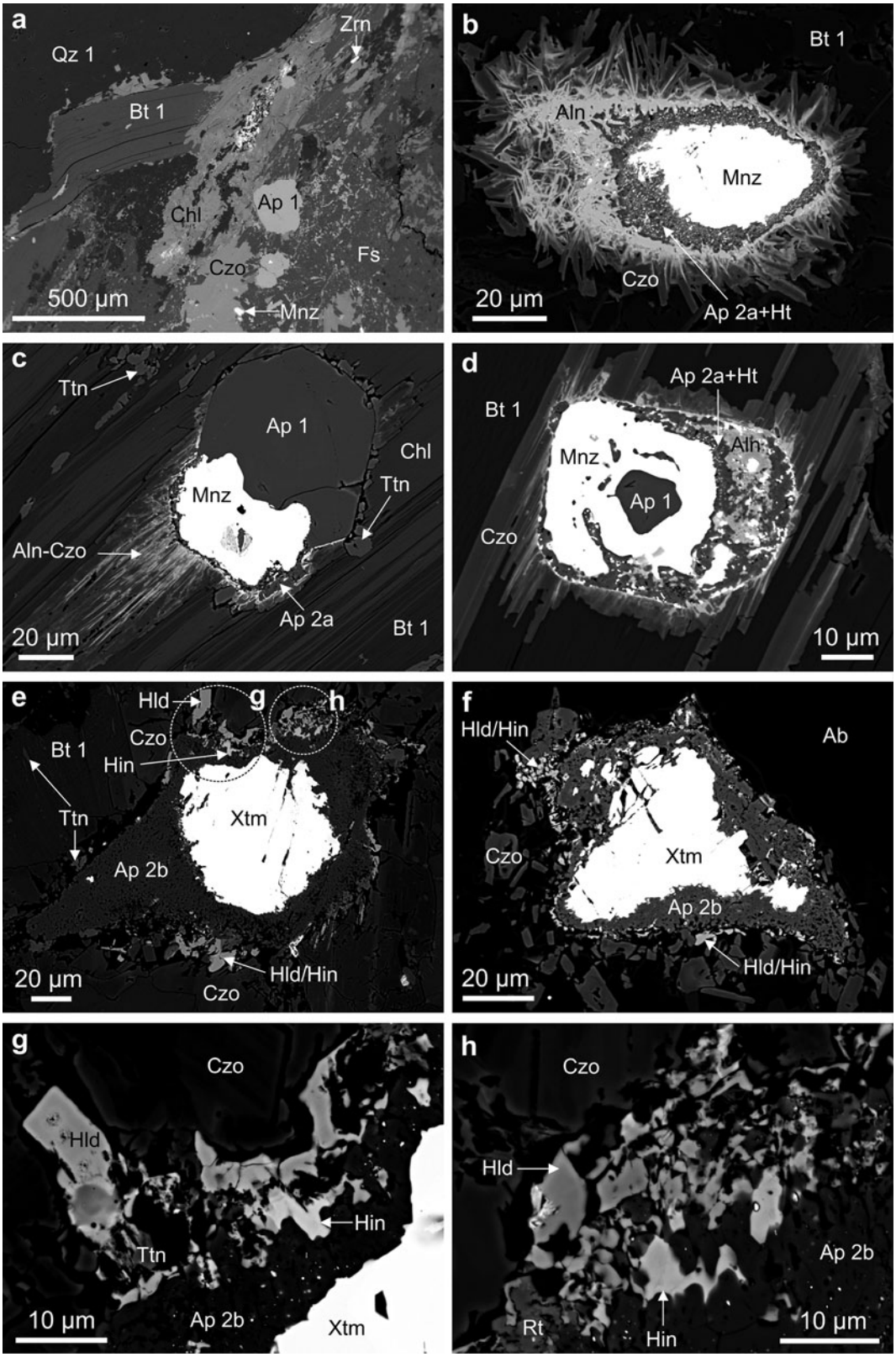

Fig. 2. Back-scattered electron (BSE) images of a mylonitised metagranite and coronae around REE accessory phosphate minerals. (a) An assemblage of rock-forming minerals including quartz-1 (Qz 1), biotite-1 (Bt 1) to chlorite (Chl), feldspars (Fs), locally replaced by fine-crystalline white mica and clinozoisite (Czo). Accessory minerals are apatite-1 (Ap 1), zircon (Zrn) and monazite-(Ce) (Mnz). (b) Typical retrograde corona around monazite-(Ce) (Mnz) surrounded by polygonal apatite-2a (Ap 2a) + bright huttonite inclusions (Ht) and epitaxial intergrowths of allanite-(Ce) (Aln) to clinozoisite (Czo) in biotite-1 (Bt 1). (c) Lopsided corona with an asymmetric tail of allanite-(Ce)-clinozoisite (Aln-Czo) trailing outwards from the monazite-(Ce) (Mnz) in close association with apatite-1 (Ap 1). The other secondary minerals are apatite-2a (Ap 2a) and titanite (Ttn). The host rock-forming minerals are biotite-1 (Bt 1) to chlorite (Chl). (d) A tiny collar of allanite-(Ce) ± monazite-(Ce) relics outlining the euhedral habit of the former intergrown apatite-1 (Ap 1) and monazite-(Ce) (Mnz). The other secondary minerals are apatite-2a (Ap 2a) + Th-silicate huttonite (Ht) and clinozoisite (Czo). The host rock-forming mineral is biotite-1 (Bt 1). (e) Secondary corona with preserved xenotime-(Y) relic (Xtm) in the central part surrounded

https://doi.org/10.1180/mgm.2022.7 Published online by Cambridge University Press

Table 1. Whole-rock compositions of the Fabova Hoľa metagranite (sample FAH-3).

Sample	FAH-3				
SiO_2 (wt. %)	69.91	Be (ppm)	3.0	Th	11.0
TiO_2	0.40	B	15*	U	2.4
Al_2O_3	15.54	Rb	120	Sc	5.0
FeO_{tot}	2.29	Cs	6.0	Y	13.4
MnO	0.06	Sr	325	La	28.5
MgO	0.95	Ba	751	Ce	60.3
CaO	1.78	Ga	21	Pr	6.89
Na_2O	4.27	Zr	155	Nd	26.6
K_2O	3.38	Hf	4.7	Sm	5.17
P_2O_5	0.15	Sn	4.0	Eu	0.84
L.O.I.	0.90	V	33	Gd	4.17
Total	99.63	Nb	10.1	Tb	0.58
		Ta	0.8	Dy	2.91
		W	8.4	Ho	0.49
A/CNK	1.12	Co	4.5	Er	1.20
A/NK	1.45	Ni	1.7	Tm	0.19
		Zn	49	Yb	1.12
		Pb	19	Lu	0.16

* Boron content from Marsina *et al.* (1999).

hellandite–(Y)-hingganite-(Y) zone is a typical feature and contrasts with the conspicuous development of the REE-bearing zone around monazite-(Ce).

Xenotime-(Y) has a distinct dominance of Y over other HREE components and the chondrite-normalised REE distribution pattern shows a HREE>LREE slope ($La_N/Yb_N = 0.001$) (Fig. 3). The relatively low, though homogeneous, distribution of B is confirmed by X-ray compositional mapping (Fig. 5). This systematic presence of B together with a slightly increased signal of Nb + Ta in xenotime-(Y), indicates the possible, but very limited schiavinatoite ($NbBO_4$) + béhierite ($TaBO_4$) substitution mechanism: $(Nb,Ta)BY_{-1}P_{-1}$.

The apatite-2b generation differs slightly from apatite-2a in REE and Y concentrations, where apatite-2b has a higher $HREE_2O_3$ and an especially higher Y_2O_3 content (average value 0.80 wt.%; 0.03 apfu HREE + Y), although the LREE content is below the EPMA detection limit. In contrast, the measured concentrations of Th and U in apatite-2b are lower than apatite-2a, with ≤0.5 wt.% $(Th,U)O_2$ (≤0.01 apfu Th and U) (Table 2).

The hellandite-(Y) compositions (Table 3) show a predominance of Y (22.9–27.8 wt.% Y_2O_3; 2.2–2.4 apfu Y) over other REE (⩽15.9 wt.% REE_2O_3; 0.92 apfu REE*)* and have an atomic ratio of $Y/(Y + REE) = 0.70–0.81$. Among the REE, hellandite-(Y) has HREE>LREE, which is also visible in the chondrite-normalised REE pattern, in accordance with its Y dominance (Fig. 3). This HREE>>LREE slope (average $La_N/Yb_N = 0.004$) is observed typically in other Y-dominant REE minerals and is analogous to the primary xenotime-(Y). Aluminium dominates strongly over Fe^{3+} among the *Z* site cations (4.1–5.3 wt.% Al_2O_3; 0.77–1.0 apfu Al and 0.0–1.4 wt.% Fe_2O_3; 0.0–0.20 apfu Fe respectively) with an atomic ratio of $Al/(Al + Fe) = 0.84–1.00$. Calcium is the dominant cation at the *X* site, ranging from 14.6 to 16.7 wt.% CaO (2.8–2.9 apfu Ca). However, all analytical results include a small Ca deficiency compared to the ideal formula, and this imbalance is compensated by an appropriate amount of REE. As a consequence, hellandite-(Y) compositions are close to the end-member formula with a small $Fe^{3+}Al_{-1}$ substitution. Other possible exchange vectors are negligible (Fig. 6).

The hingganite-(Y) composition (Table 4) shows a dominance of Y (26.7–33.4 wt.% Y_2O_3; 1.0–1.3 apfu Y) over other REE, mainly HREE (10.2–15.1 wt.% REE_2O_3; 0.23–0.38 apfu REE) on the *A* site. The atomic ratio of Y/(Y + REE) for hingganite-(Y) (0.77–0.82) is similar, though in a narrower range compared to hellandite-(Y). In addition, the chondrite-normalised REE pattern shows an identical trend with the enrichment of HREE (slope ($La_N/Yb_N = 0.006$) (Fig. 3). Additionally, Ca is the other significant cation at the *A* site (4.5–10.6 wt.% CaO; 0.36–0.79 apfu Ca), which indicates the significant presence of datolite $[Ca_2\square B_2Si_2O_8(OH)_2]$ and homilite $(Ca_2Fe^{2+}B_2Si_2O_8O_2)$ molecules (Fig. 7). Hingganite-(Y) has a dominant vacancy (0.49–0.65 pfu) over the *M* site cations, especially the Fe content, which is markedly low (5.5–7.8 wt.% FeO; 0.34–0.50 apfu Fe) with a Fe/(Fe + vacancy) atomic ratio of 0.34–0.51. Conversely, hingganite-(Y) has a negligible and usually zero Al content at the *M* site, thereby indicating a strong Al and Fe distinction between hellandite-(Y) and hingganite-(Y). Whereas hellandite-(Y) has an almost constant B content (cf. Oberti *et al.*, 2002; Miyawaki *et al.*, 2015), the B concentration in hingganite-(Y) from the Fabova Hoľa metagranite is controlled by the datolite $CaB(REE)_{-1}Be_{-1}$ substitution with $B/(B + Be)_{calc} = 0.0–0.38$. It has an intermediate solid solution between the Be-dominant [hingganite-(Y)–gadolinite-(Y)], and B-dominant (homilite, datolite) end-members of the gadolinite-group minerals.

Raman spectra of hellandite-(Y) and hingganite-(Y)

The presence of B- and Be-bearing silicate phases in the breakdown products was determined from their Raman spectra. The Raman spectra of the hingganite-(Y) can be divided into several regions with relatively intensive bands and these vary due to different crystal orientations (Fig. 8a). In the region between 100 and 400 cm^{-1}, the most prominent peaks are at 189 cm^{-1} (with a peak on the shoulder at 153 cm^{-1}) and 324 cm^{-1}. The region of 400 to 800 cm^{-1} includes several overlapping, less-intensive bands with two prominent peaks at 453 and 639 cm^{-1}. The third most intensive peak, together with 189 and 639 cm^{-1}, is located at 917 cm^{-1} with two shoulder peaks at 969 and 998 cm^{-1}. In the high-frequency region, there is a sharp peak at 3546 cm^{-1} located on the broad band spreading between 3100 and 4000 cm^{-1}.

All μ-Raman depolarised spectra of randomly oriented hellandite-(Y) crystals (FAH-3) correspond to their minor compositional variations. In the low-frequency region (200−1000 cm^{-1}), the spectra show numerous peaks superimposed on an increased background luminescence. The most dominant features are in the regions of 250−370, 500−550, and 560−750 cm^{-1} (Fig. 8b–d), in addition to the complexes of numerous, less-intensive bands. Two relatively sharp peaks at 3454 and 3662 cm^{-1} located on top of the broad band are present in the high-frequency region. (Fig. 8d).

by an apatite-2b zone (Ap 2b). The external zone consists of hellandite-(Y) (Hld), hingganite-(Y) (Hin) and clinozoisite (Czo). The host rock-forming mineral is biotite-1 (Bt 1) with tiny inclusions of titanite (Ttn). (f) A similar corona with a central xenotime-(Y) relic (Xtm). A satellite chain-like aggregate of hellandite-(Y) (Hld) and hingganite-(Y) (Hin) is positioned between the apatite-2b zone (Ap 2b) and the distal zone of clinozoisite (Czo). The host rock-forming mineral is albite (Ab). (g) Close-up of the encircled area in (e) with hellandite-(Y) (Hld) and hingganite-(Y) (Hin) crystals in close vicinity to primary xenotime-(Y) (Xtm). The other secondary minerals are apatite-2b (Ap 2b), clinozoisite (Czo) and titanite (Ttn). (h) Close-up of the encircled area in (e) with hellandite-(Y) (Hld) and hingganite-(Y) (Hin) crystals in association with secondary apatite-2b (Ap 2b), clinozoisite (Czo) and rutile (Rt). IMA–CNMNC approved mineral symbols according to Warr (2021).

https://doi.org/10.1180/mgm.2022.7 Published online by Cambridge University Press

Table 2. Representative EPMA compositions of monazite-(Ce), xenotime-(Y), fluorapatite and epidote-group minerals (in wt.% and apfu). Abbreviations are as follows: monazite-(Ce) (Mnz), xenotime-(Y) (Xtm), fluorapatite (Ap), allanite-(Ce) (Aln), epidote (Ep), clinozoisite (Czo).

	Mnz	Mnz	Xtm	Xtm	Ap 2a	Ap 2a	Ap 2b	Ap 2b		Aln	Ep	Czo
Wt.%												
SO_3	0.03	0.04	0.00	0.00	0.01	0.01	0.00	0.01	SiO_2	30.66	36.91	38.80
P_2O_5	29.72	28.73	35.31	34.80	40.78	41.13	41.57	40.95	TiO_2	0.41	2.44	0.15
As_2O_5	0.18	0.00	0.01	0.05	0.00	0.06	0.02	0.00	ThO_2	0.25	0.00	0.01
Nb_2O_5	n.a.	n.a.	0.04	0.03	n.a.	n.a.	n.a.	n.a.	UO_2	0.01	0.00	0.00
Ta_2O_5	n.a.	n.a.	0.00	0.00	n.a.	n.a.	n.a.	n.a.	Al_2O_3	15.99	19.83	26.82
SiO_2	0.42	0.78	0.32	0.56	0.42	0.52	0.51	0.38	Y_2O_3	0.00	0.09	0.04
ThO_2	4.01	8.39	0.10	0.69	0.62	0.01	0.08	0.14	La_2O_3	6.44	0.16	0.02
UO_2	0.11	0.70	1.75	1.37	0.01	0.04	0.03	0.07	Ce_2O_3	12.81	0.32	0.05
Al_2O_3	0.00	0.00	0.00	0.00	n.a.	n.a.	n.a.	n.a.	Pr_2O_3	1.20	0.15	0.10
Y_2O_3	1.05	2.98	42.95	43.13	0.11	0.49	0.71	0.50	Nd_2O_3	4.63	0.21	0.05
La_2O_3	13.79	10.55	0.01	0.02	0.68	0.04	n.a.	n.a.	Sm_2O_3	0.44	0.07	0.02
Ce_2O_3	29.10	24.08	0.09	0.05	1.47	0.21	n.a.	n.a.	Eu_2O_3	0.26	0.39	0.27
Pr_2O_3	3.34	3.11	0.01	0.03	0.09	0.12	n.a.	n.a.	Gd_2O_3	0.11	0.10	0.08
Nd_2O_3	12.85	11.73	0.27	0.46	0.75	0.22	n.a.	n.a.	Tb_2O_3	0.00	0.03	0.04
Sm_2O_3	2.05	2.92	0.56	0.61	0.10	0.06	0.08	0.03	Dy_2O_3	0.00	0.03	0.02
Eu_2O_3	0.09	0.12	0.02	0.01	n.a.	0.07	n.a.	n.a.	Ho_2O_3	0.05	0.00	0.00
Gd_2O_3	1.18	1.84	1.35	1.61	0.12	0.07	0.00	0.17	Er_2O_3	0.00	0.19	0.15
Tb_2O_3	0.07	0.20	0.57	0.57	n.a.	0.09	0.00	0.00	Tm_2O_3	0.01	0.04	0.04
Dy_2O_3	0.34	0.81	5.41	5.61	n.a.	0.11	0.10	0.11	Yb_2O_3	0.05	0.06	0.05
Ho_2O_3	0.04	0.05	1.06	1.15	n.a.	0.00	0.00	0.00	Lu_2O_3	0.01	0.07	0.00
Er_2O_3	0.33	0.45	3.77	3.98	n.a.	0.28	0.07	0.05	Fe_2O_3	2.52	12.28	7.75
Tm_2O_3	0.11	0.12	0.75	0.67	n.a.	0.02	n.a.	n.a.	FeO	10.53	2.19	0.74
Yb_2O_3	0.10	0.14	3.87	3.05	n.a.	0.06	0.099	0.06	MgO	0.15	0.00	0.00
Lu_2O_3	0.07	0.14	1.09	0.97	n.a.	0.02	0.05	0.09	MnO	0.27	0.27	0.20
FeO_t	0.04	0.00	0.20	0.23	0.59	0.49	0.25	0.45	PbO	0.04	0.00	0.00
MnO	n.a.	n.a.	n.a.	n.a.	0.04	0.12	0.00	0.00	BaO	0.00	0.01	0.01
PbO	0.07	0.16	0.12	0.09	0.02	0.00	0.01	0.05	SrO	0.00	0.43	0.22
BaO	n.a.	n.a.	n.a.	n.a.	0.00	0.00	0.04	0.08	CaO	10.73	22.55	23.28
SrO	0.01	0.03	0.00	0.00	0.00	0.02	0.00	0.00	Na_2O	0.00	0.00	0.02
CaO	0.91	1.44	0.33	0.36	51.53	53.71	54.18	53.68	F	0.16	0.00	0.00
Na_2O	n.a.	n.a.	n.a.	n.a.	0.02	0.05	0.00	0.01	Cl	0.00	0.01	0.01
F	n.a.	n.a.	n.a.	n.a.	3.51	3.68	3.72	3.65	O=F	−0.08	0.00	0.00
Cl	n.a.	n.a.	n.a.	n.a.	n.a.	0.02	0.02	0.02	O=Cl	0.00	0.00	0.00
O=F	-	-	-	-	−1.48	−1.55	−1.57	−1.54	H_2O^*	1.54	1.85	1.92
O=Cl	-	-	-	-	-	0.00	0.00	0.00	Total	99.18	100.65	100.86
H_2O^*	-	-	-	-	0.05	0.02	0.00	0.02				
Total	100.01	99.48	99.93	100.09	99.45	100.20	99.96	98.98				

	Mnz	Mnz	Xtm	Xtm	Ap 2a	Ap 2a	Ap 2b	Ap 2b		Aln	Ep	Czo
Apfu												
S^{6+}	0.001	0.001	0.000	0.000	0.001	0.000	0.000	0.001	Si^{4+}	2.991	2.998	3.024
P^{5+}	0.984	0.964	0.996	0.982	3.020	2.955	2.993	2.966	Al^{3+}	0.009	0.001	0.000
As^{5+}	0.004	0.000	0.000	0.001	0.000	0.003	0.001	0.000	ΣT	3.000	3.000	3.024
Si^{4+}	0.017	0.031	0.011	0.019	0.037	0.044	0.043	0.032	Al^{3+}	1.000	1.000	1.000
ΣA, ΣT	1.005	0.996	1.007	1.002	3.058	3.002	3.037	2.999	Fe^{3+}	0.000	0.000	0.000
Nb^{5+}	-	-	0.000	0.000	-	-	-	-	$\Sigma M2$	1.000	1.000	1.000
Ta^{5+}	-	-	0.000	0.000	-	-	-	-	Fe^{3+}	0.097	0.750	0.455
Th^{4+}	0.036	0.076	0.001	0.005	0.012	0.000	0.002	0.003	Al^{3+}	0.000	0.083	0.484
U^{4+}	0.001	0.006	0.013	0.010	0.000	0.001	0.001	0.001	Fe^{2+}	0.859	0.148	0.048
Al^{3+}	0.000	0.000	0.000	0.000	-	-	-	-	Mg^{2+}	0.022	0.000	0.000
Y^{3+}	0.022	0.063	0.762	0.765	0.005	0.022	0.032	0.023	Mn^{2+}	0.022	0.018	0.013
La^{3+}	0.199	0.154	0.000	0.000	0.022	0.001	-	-	$\Sigma M3$	1.000	1.000	1.000
Ce^{3+}	0.417	0.349	0.001	0.001	0.047	0.007	-	-	Ti^{4+}	0.030	0.149	0.009
Pr^{3+}	0.048	0.045	0.000	0.000	0.003	0.004	-	-	Fe^{3+}	0.089	0.000	0.000
Nd^{3+}	0.179	0.166	0.003	0.006	0.023	0.007	-	-	Al^{3+}	0.829	0.814	0.980
Sm^{3+}	0.028	0.040	0.006	0.007	0.003	0.002	0.002	0.001	$\Sigma M1$	0.948	0.963	0.988
Eu^{3+}	0.001	0.002	0.000	0.000	-	0.002	-	-	Ca^{2+}	1.000	1.000	0.996
Gd^{3+}	0.015	0.024	0.015	0.018	0.003	0.002	0.000	0.005	Na^{+}	0.000	0.000	0.004
Tb^{3+}	0.001	0.003	0.006	0.006	-	0.002	0.000	0.000	$\Sigma A1$	1.000	1.000	1.000
Dy^{3+}	0.004	0.010	0.058	0.060	-	0.003	0.003	0.003	Th^{4+}	0.005	0.000	0.000
Ho^{3+}	0.001	0.001	0.011	0.012	-	0.000	0.000	0.000	U^{4+}	0.000	0.000	0.000
Er^{3+}	0.004	0.006	0.039	0.042	-	0.007	0.002	0.001	Y^{3+}	0.000	0.004	0.002
Tm^{3+}	0.001	0.001	0.008	0.007	-	0.000	-	-	La^{3+}	0.232	0.005	0.001
Yb^{3+}	0.001	0.002	0.039	0.031	-	0.002	0.003	0.002	Ce^{3+}	0.458	0.009	0.001
Lu^{3+}	0.001	0.002	0.011	0.010	-	0.001	0.001	0.002	Pr^{3+}	0.043	0.005	0.003
Fe^{2+}	0.001	0.000	0.005	0.006	0.043	0.035	0.017	0.032	Nd^{3+}	0.161	0.006	0.001
Mn^{2+}	-	-	-	-	0.003	0.009	0.000	0.000	Sm^{3+}	0.015	0.002	0.000

(*Continued*)

https://doi.org/10.1180/mgm.2022.7 Published online by Cambridge University Press

Table 2. (*Continued.*)

	Mnz	Mnz	Xtm	Xtm	Ap 2a	Ap 2a	Ap 2b	Ap 2b		Aln	Ep	Czo
Pb^{2+}	0.001	0.002	0.001	0.001	0.000	0.000	0.000	0.001	Eu^{3+}	0.009	0.011	0.007
Ba^{2+}	-	-	-	-	0.000	0.000	0.001	0.003	Gd^{3+}	0.003	0.003	0.002
Sr^{2+}	0.000	0.001	0.000	0.000	0.000	0.001	0.000	0.000	Tb^{3+}	0.000	0.001	0.001
Ca^{2+}	0.038	0.061	0.012	0.013	4.830	4.884	4.936	4.921	Dy^{3+}	0.000	0.001	0.001
Na^{+}	-	-	-	-	0.003	0.009	0.000	0.002	Ho^{3+}	0.001	0.000	0.000
Σ*B*, Σ*M*	0.998	1.012	0.993	1.001	5.000	5.000	5.000	5.000	Er^{3+}	0.000	0.005	0.004
OH^{-}_{calc}	-	-	-	-	0.028	0.010	0.000	0.010	Tm^{3+}	0.000	0.001	0.001
F^{-}	-	-	-	-	0.972	0.988	1.000	0.988	Yb^{3+}	0.001	0.002	0.001
Cl^{-}	-	-	-	-	-	0.002	0.002	0.002	Lu^{3+}	0.000	0.002	0.000
Σ*X*	-	-	-	-	1.000	1.000	1.003	1.000	Pb^{2+}	0.001	0.000	0.000
X_{hut}	0.017	0.031	-	-	-	-	-	-	Ba^{2+}	0.000	0.000	0.000
X_{chrl}	0.058	0.111	-	-	-	-	-	-	Sr^{2+}	0.000	0.020	0.010
X_{mnz}	0.925	0.859	-	-	-	-	-	-	Ca^{2+}	0.122	0.962	0.953
									Σ*A*2	1.052	1.037	0.988
									Σcat.	7.999	8.000	8.000
									$(F, Cl)^{-}$	0.000	0.000	0.000
									OH^{-}	1.000	1.000	1.000

*H_2O contents calculated on the basis of ideal stoichiometry. n.a. = not analysed, - = not calculated. 0.00 wt.% values indicate below the detection limit.

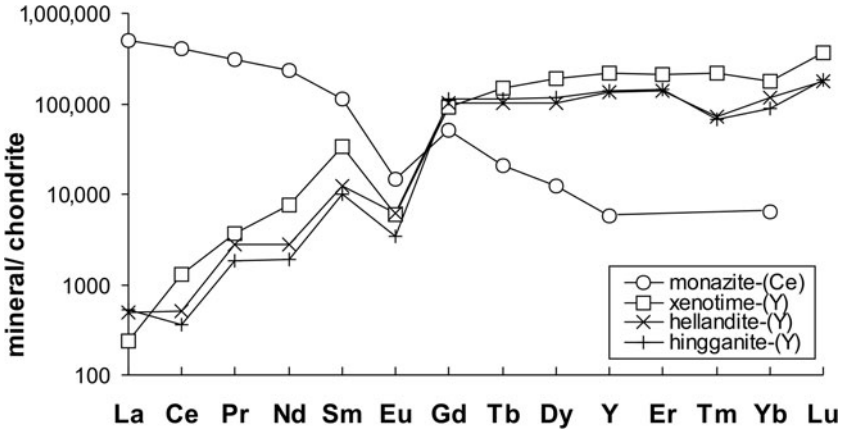

Fig. 3. Average chondrite normalised REE distribution patterns of REE-bearing minerals. Normalised values from Barrat *et al.* (2012). Note: Tb_N in the Y–B–Be silicates is interpolated between Gd_N and Dy_N due to a probable EPMA artefact. Yttrium is plotted in the position of Ho.

Discussion and conclusions

Raman spectra interpretation

Raman spectra of the investigated hingganite-(Y) were interpreted in context with published data, including that of isostructural datolite and gadolinite (Frost *et al.*, 2013; Goryainov *et al.*, 2015; Thomas and Davidson, 2017; Škoda *et al.*, 2018; Paulmann *et al.*, 2019; Gorelova *et al.*, 2020; Tomašić *et al.*, 2020) and were also compared with spectra of macroscopic gadolinite samples. Škoda *et al.* (2018) assigned bands in the region of 200–750 cm^{-1} to bending modes of Si–O and Be–O, stretching vibrations of REE–O and Fe–O, as well as to lattice vibrations. According to Hofmeister *et al.* (1987), modes below 350 cm^{-1} in silicates are generally considered to be translations. The Raman band at 3546 cm^{-1} is attributed to stretching vibrations of OH^{-} units in the mineral structure (Fig. 8*a*).

Part of the bands in the region from 450 cm^{-1} to 650 cm^{-1} could be assigned to bending vibrations of the layer formed by $(SiO_4)^{4-}$ and $(BeO_4)^{6-}$ tetrahedra and were also detected in the spectra of macroscopic samples (Gorelova *et al.*, 2020). Raman peaks at 969 cm^{-1} and 917 cm^{-1} (in the range of 969–992 and 906–917 cm^{-1} in the fitted spectra) are assigned to stretching vibrations of Si–O and Be–O in tetrahedral coordination (Škoda *et al.*, 2018; Gorelova *et al.*, 2020). The presence of a peak at 917 cm^{-1} correlates well with the fitted spectra of the macroscopic gadolinite samples. Weak Raman bands in the range of 650–800 cm^{-1} correspond to Be–O stretching vibrations (Hofmeister *et al.*, 1987).

However, not all the bands can easily be attributed to known causes, according to the published data (Leite *et al.*, 2001; Škoda *et al.*, 2018; Gorelova *et al.*, 2020). The Raman spectra of all the measured mineral phases, compositionally corresponding to hingganite-(Y), are essentially obscured by strong photoluminescence, as both broad and narrow bands. Even a minor lanthanoid content in the structure may cause intense luminescence (Panczer *et al.*, 2012; Lenz *et al.*, 2015; Gaft *et al.*, 2005; de Bettencourt-Dias, 2014). Taking into consideration the concentrations of Gd, Dy, Eu, Yb, Lu and Tm (Table 4), there is a strong indication that some of features in the spectra are in fact photoluminescence bands. Some of these bands can be present in the range of 453–562 cm^{-1} in the 532 nm spectrum of hingganite-(Y). If recalculated to wavelength, 540–550 nm bands could correspond to luminescence bands that were caused by the $^4S_{3/2}$–$^4I_{15/2}$ electronic transition in Er^{3+} (Bodył *et al.*, 2009; de Bettencourt-Dias, 2014).

The presence of 3546 cm^{-1} correlates well with the hingganite-(Y) composition, which contains the OH^{-} group located at the φ5 site, in contrast to gadolinite, which contains O at φ5 (Bačík *et al.*, 2017). However, the peak is located on the top of the strong broad band (Fig. 8*a*), which was recalculated, considering that the 532 nm excitation has a centre at ca. 660 nm

https://doi.org/10.1180/mgm.2022.7 Published online by Cambridge University Press

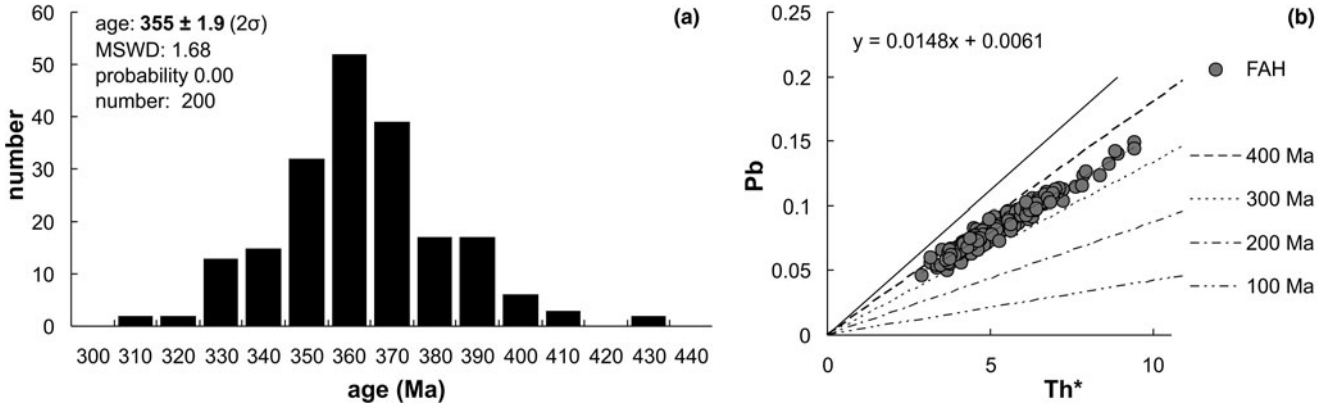

Fig. 4. Th–U–total Pb EPMA age determination. (a) Histogram and (b) isochron diagram of monazite ages from the Fabova hoľa granitoids. Pb values are in wt.%, Th* = Th + 3.15*U wt.%.

and therefore, can be interpreted as a luminescence band induced by the $^4F_{9/2}\rightarrow{}^6H_{15/2-9/2}$ electronic transition in Dy^{3+} (de Bettencourt-Dias, 2014).

The stacked spectra of hellandite-(Y) measured with 532 nm and 633 nm excitation show several overlapping peaks that might be attributed to Raman scattering. The shape and band intensities of individual spectra vary due to different crystal orientation. The position of the broad bands partly matches the spectrum of hellandite-(Ce) (RRUFF ID: R061013, Lafuente *et al.*, 2015), where the tetrahedrally coordinated *T* site is vacant. The high number and broadening of the bands results from a varying composition. In the Raman spectra, as in the gadolinite-group minerals, stretching vibrations of REE–O and Fe–O and lattice vibrations are observed in the spectral region 200–750 cm^{-1} (Leite *et al.*, 2001; Škoda *et al.*, 2018). The vibrations in the 320–600 cm^{-1} region may be attributed to out-of-plane and in-plane bending vibrations of the $(SiO_4)^{4-}$ tetrahedron. Hofmeister *et al.* (1987) assigned the wavenumbers of the Si–O and Be–O vibrations in phenakite (Be_2SiO_4), which is a mineral with $(SiO_4)^{4-}$ and $(BeO_4)^{6-}$ tetrahedra and roughly analogous to the layers of tetrahedra in hellandite. The observed bands above 875 cm^{-1} thus correspond to Si–O antisymmetric stretching vibrations. Raman bands at 780–810 cm^{-1} and 768–778 cm^{-1} may possibly relate to Si–O and Be–O stretching vibrations, respectively. The band intensity at 662 cm^{-1} (in 633 nm excited spectrum) can be influenced by photoluminescence of Dy^{3+}, which occurs in some minerals at ~660 nm (Gaft *et al.*, 2005; de Bettencourt-Dias, 2014). This luminescence band results from the $^4F_{9/2}\rightarrow{}^6H_{15/2-9/2}$ electronic transition in Dy^{3+}, similarly as in hingganite-(Y) (de Bettencourt-Dias, 2014). In the range of 2500–4000 cm^{-1} spectra possess continuum background topology.

The strong broad band below the two intensive lines at 3454 cm^{-1} and 3662 cm^{-1} was only detected with 532 nm excitation. The relatively sharp bands could be attributed to OH^- vibrations. Della Ventura *et al.* (2002) described spectral bands in this region as an expression of a wide variety of OH^- environments due to local short-range disorder at the next-nearest-neighbour cation sites bonded to O5. However, the broad band with a position similar to the 532 nm spectrum of hingganite-(Y) can also result in the $^4F_{9/2}\rightarrow{}^6H_{15/2-9/2}$ electronic transition in Dy^{3+} (de Bettencourt-Dias, 2014).

On the basis of our interpretations, Er and Dy are the main sources of photoluminescence features in the spectra of both hingganite-(Y) and hellandite-(Y). This correlates perfectly with the chemical data. Erbium and Dy are the most abundant REE together with Gd and Yb. However, the most prominent photoluminescence band of Gd^{3+} ($^6F_{7/2}\rightarrow{}^8S_{7/2}$) is in the UV region around 315 nm, and the most emissive $^2F_{5/2}\rightarrow{}^2H_{7/2}$ electronic transition of Yb^{3+} manifests itself in the NIR region around 980 nm (de Bettencourt-Dias 2014). The ranges of measurement were 535 to 675 nm and 640 to 855 nm for the 532 and 633 nm excitations, respectively. The content of other REE with possible photoluminescence bands in the measured region (Pr, Sm, Eu, Tb, Ho and Tm; de Bettencourt-Dias, 2014) are lower, usually below 0.5 oxide wt.%. Therefore, these REE may contribute to the dominant photoluminescence features, or to an increase in the background, however they do not manifest in a resolvable photoluminescence band.

Crystal chemistry of contrasting coronae formation and breakdown reactions

The metamorphic-hydrothermal breakdown of monazite-(Ce) to the secondary fluorapatite–allanite-(Ce)–clinozoisite corona is a widely reported process in granitic, gneissic and metapelitic lithologies during post-magmatic cooling, or low- to high-grade prograde/retrograde metamorphic conditions (Broska and Siman, 1998; Finger *et al.*, 1998, 2016; Broska *et al.*, 2005; Majka and Budzyń, 2006; Petrík and Konečný, 2009; Ondrejka *et al.*, 2012, 2016; Regis *et al.*, 2012; Upadhay and Pruseth, 2012; Lo Pò *et al.*, 2016; Hentschel *et al.*, 2020). It has also been experimentally replicated (Budzyń *et al.*, 2011, 2017). The analogous breakdown of xenotime-(Y) is not as common as monazite, but, when present, it usually results in similar corona structures, with an inner zone of fluorapatite (commonly HREE +Y-rich) and/ or an outer zone of HREE-bearing epidote-group minerals, albeit in much smaller amounts (Broska *et al.*, 2005; Majka and Budzyń, 2006; Janots *et al.*, 2008; Broska and Petrík, 2015; Budzyń *et al.*, 2018; Hentschel *et al.*, 2020). Experiments involving xenotime-(Y) replacement indicate that the reaction products are roughly similar to those found in natural occurrences over a wide *P*–*T* range, and reflect the relatively high mobilisation of HREE+Y into the apatite-supergroup minerals (fluorapatite, fluorcalciobritholite) or epidote, which depends on the CaO/Na_2O ratio (Budzyń and Kozub-Budzyń, 2015; Budzyń *et al.*, 2017). These experiments also suggest that the reactivity of xenotime-(Y) is temperature-dependent, and that the stability of xenotime-(Y) and HREE+Y-rich epidote is strongly controlled

https://doi.org/10.1180/mgm.2022.7 Published online by Cambridge University Press

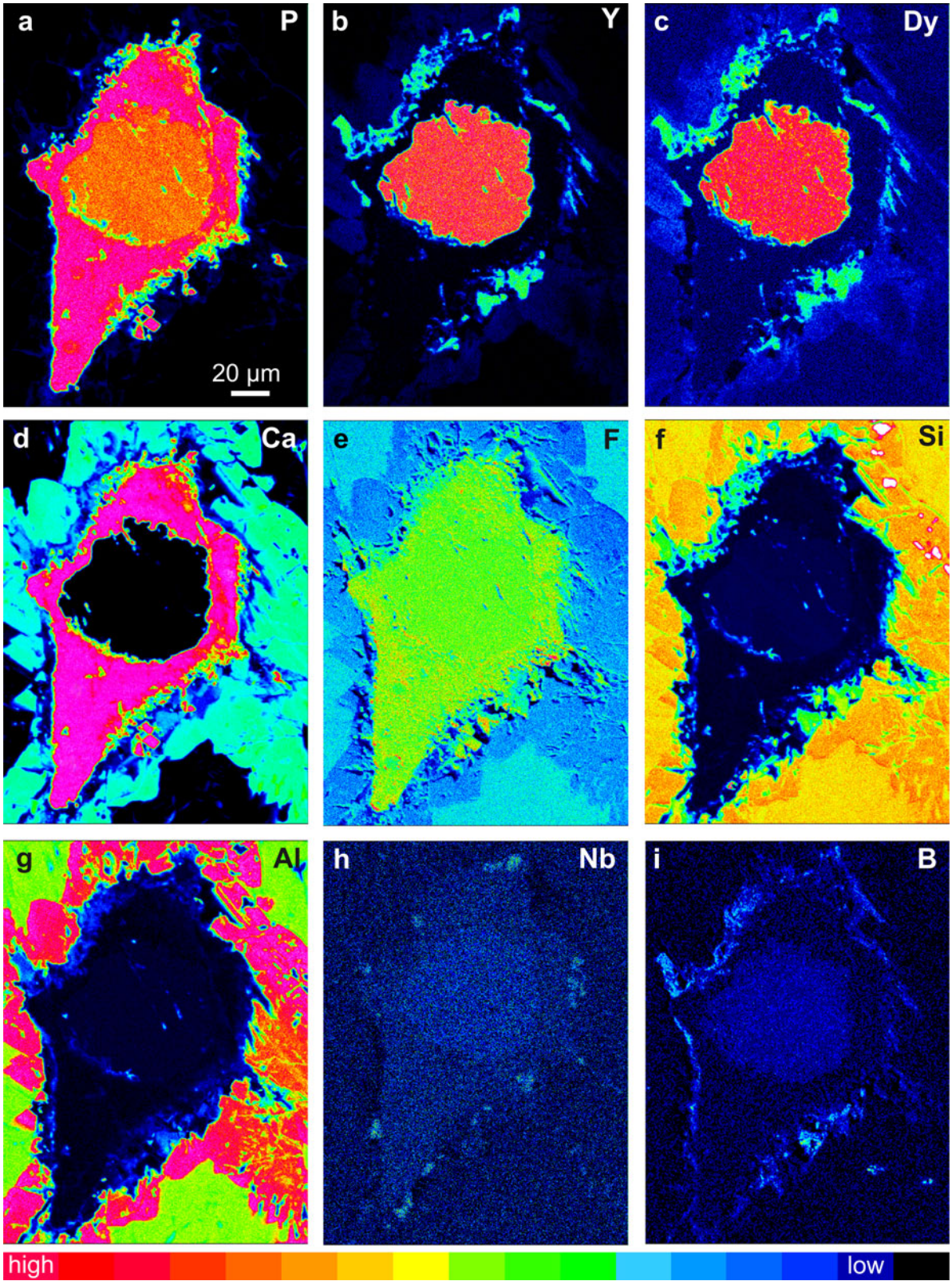

Fig. 5. False colour X-ray map showing the distribution of elements in the reaction corona around xenotime-(Y).

by pressure (Budzyń *et al.*, 2017). These results suggest that xenotime-(Y) is more stable than monazite-(Ce) due to a lesser mobility of HREE+Y compared with LREE during low- to medium-grade metamorphism.

The effects of retrograde metamorphism during, and after, deformation on primary magmatic monazite-(Ce) and xenotime-(Y) are distinctive in the Fabova Hoľa metagranites. Similar corona reaction zones around monazite-(Ce) and

https://doi.org/10.1180/mgm.2022.7 Published online by Cambridge University Press

Table 3. Representative compositions from EPMA of hellandite-(Y) (in wt.% and apfu).

Wt.%	FAH-3a			FAH-3j		Apfu	FAH-3a			FAH-3j	
SiO_2	23.83	24.01	23.71	24.13	23.99	Si^{4+}	4.000	4.000	4.000	4.000	4.000
TiO_2	0.24	0.26	0.02	0.17	0.02	Ti^{4+}	0.030	0.032	0.002	0.021	0.002
ThO_2	0.00	0.05	0.01	-	0.01	Al^{3+}	0.924	0.947	0.889	0.867	0.851
UO_2	0.07	0.10	0.09	0.05	0.05	Fe^{3+}	0.107	0.085	0.087	0.115	0.095
B_2O_3*	13.80	13.91	13.73	13.98	13.90	Mn^{3+}**	0.000	0.000	0.022	0.000	0.052
Al_2O_3	4.67	4.82	4.47	4.44	4.33	ΣZ	1.061	1.064	1.000	1.002	1.000
Y_2O_3	26.63	26.56	26.81	27.33	26.74	B^{3+}*	4.000	4.000	4.000	4.000	4.000
La_2O_3	0.03	-	0.04	0.01	-	Th^{4+}	0.000	0.002	0.000	0.000	0.000
Ce_2O_3	0.01	0.01	0.04	-	-	U^{4+}	0.003	0.004	0.003	0.002	0.002
Pr_2O_3	-	-	0.09	0.01	0.01	Y^{3+}	2.379	2.354	2.407	2.411	2.373
Nd_2O_3	0.02	0.09	0.07	0.03	0.07	La^{3+}	0.002	0.000	0.002	0.001	0.000
Sm_2O_3	-	0.05	0.19	0.11	0.01	Ce^{3+}	0.000	0.000	0.002	0.000	0.000
Eu_2O_3	0.00	0.00	0.00	0.04	0.07	Pr^{3+}	0.000	0.000	0.005	0.001	0.001
Gd_2O_3	1.99	1.94	1.90	1.87	1.85	Nd^{3+}	0.001	0.006	0.004	0.002	0.004
Tb_2O_3	0.04	-	-	-	-	Sm^{3+}	0.000	0.003	0.011	0.006	0.000
Dy_2O_3	2.60	2.59	2.74	2.33	2.81	Eu^{3+}	0.000	0.000	0.000	0.002	0.004
Ho_2O_3	0.23	0.35	0.15	0.17	0.12	Gd^{3+}	0.111	0.107	0.106	0.103	0.102
Er_2O_3	2.88	2.75	2.68	2.65	2.64	Tb^{3+}	0.002	0.000	0.000	0.000	0.000
Tm_2O_3	0.22	0.21	0.18	0.31	0.17	Dy^{3+}	0.140	0.139	0.149	0.125	0.151
Yb_2O_3	2.91	3.02	2.31	2.56	2.41	Ho^{3+}	0.012	0.018	0.008	0.009	0.006
Lu_2O_3	0.54	0.63	0.47	0.69	0.53	Er^{3+}	0.152	0.144	0.142	0.138	0.138
Fe_2O_3	0.85	0.68	0.68	0.92	0.76	Tm^{3+}	0.011	0.011	0.009	0.016	0.009
Mn_2O_3**	0.00	0.00	0.17	0.00	0.41	Yb^{3+}	0.149	0.153	0.119	0.130	0.122
MnO**	0.58	0.44	0.28	0.34	0.05	Lu^{3+}	0.027	0.032	0.024	0.035	0.027
CaO	15.93	15.94	16.46	16.47	16.43	Mn^{2+}**	0.082	0.062	0.040	0.047	0.006
H_2O***	1.81	1.91	1.86	2.00	2.19	Ca^{2+}	2.865	2.845	2.976	2.925	2.936
Total	99.86	100.32	99.12	100.59	99.54	$\Sigma X + Y$	5.938	5.881	6.009	5.952	5.882
						OH^-***	2.024	2.122	2.092	2.207	2.440

*B_2O_3 content calculated on the basis of ideal stoichiometry ** The partition of total Mn between Mn^{2+} and Mn^{3+} was calculated from ideal stoichiometry and neutral charge balance. ***H_2O content calculated from charge balance. - = not analysed/calculated. 0.00 wt.% values indicate below the detection limit.

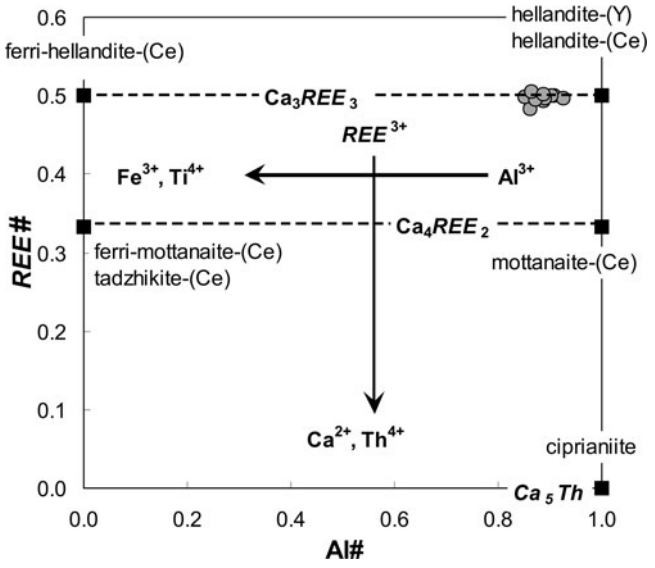

Fig. 6. Compositional diagram of the hellandite-group minerals with the principal substitution vectors and positions of the hellandite-(Y) from the Fabova Hoľa metagranite. Al# = Al/((Al + Fe^{3+} + Mn^{3+} + Ti) apfu; REE# = REE/(REE + Ca + Mn^{2+} + Th + U) apfu; REE = ∑(La + Ce + … + Lu + Y) apfu.

xenotime-(Y) usually suggest that they were most probably formed contemporaneously, and that the mechanism of their formation was similar (cf. Broska *et al.*, 2005; Majka *et al.*, 2011). In some cases, the fluorapatite–hingganite-(Y) coronae, as a product of fluid-induced breakdown of xenotime-(Y) and beryl, have been described from the Skoddefjellet pegmatite, Svalbard (Majka *et al.*, 2011), whereas the partial replacement of xenotime-(Y) by hingganite-(Y) and Y-rich allanite-(Ce) was documented in the Piława Górna pegmatite, Poland (Budzyń *et al.*, 2018). Alteration of primary monazite-(Ce) and xenotime-(Y) resulted in the formation of discrete grains of secondary hingganite-(Y) to hingganite-(Nd) in association with secondary Sr,S-rich monazite-(Ce) in the Bacúch metamorphic magnetite deposit, Veporic Unit, Slovakia (Pršek *et al.*, 2010), only ~13 km NW from the FAH-3 metagranite sample. All of these examples indicate a substantial supply of Be during the xenotime (± monazite) breakdown.

However, in our example, the REE remobilisation during alteration of the primary monazite-(Ce) and xenotime-(Y) resulted in a slightly different secondary assemblage. Whereas LREE released from the altered monazite-(Ce) were transported through the apatite-2a zone and accumulated in an allanite-(Ce) zone, the HREE and Y from xenotime-(Y) were transported the same distance, though precipitated as hellandite-(Y) and hingganite-(Y) (Fig. 9). The reported corona assemblage, which includes Y–B–Be silicates and most notably hellandite-(Y), represents a new type of breakdown micro-texture with the involvement of light elements (B and Be) in the reaction, which have not been reported previously. The metamorphic/metasomatic replacement during blastomylonitisation including fluids rich in B and Be can be expressed by the following generalised reactions:

Mnz + (Ca, Fe, Si, Al and F)-rich fluid → FAp + Ht + Aln + Czo;
Xtm + (Ca, Fe, Si, Al, F, B and Be)-rich fluid → FAp + Hld + Hin + Czo.

Hellandite-(Y), which is a relatively rare borosilicate mineral, occurs mostly as a late-magmatic to hydrothermal mineral of

https://doi.org/10.1180/mgm.2022.7 Published online by Cambridge University Press

Table 4. Representative compositions from EPMA of hingganite-(Y) from the gadolinite group (in wt.% and apfu).

Wt.%	10	11	1	6	7	Apfu	10	11	1	6	7
SiO_2	28.17	28.59	28.24	28.41	27.15	Th^{4+}	0.001	0.000	0.001	0.000	0.000
TiO_2	0.15	0.21	0.18	0.27	0.02	U^{4+}	0.002	0.001	0.001	0.001	0.001
ThO_2	0.03	-	0.07	0.01	0.01	Y^{3+}	1.050	0.993	1.081	1.027	1.261
UO_2	0.12	0.06	0.08	0.09	0.08	La^{3+}	0.001	0.000	0.000	0.000	0.000
B_2O_3*	4.87	5.96	3.59	6.02	2.63	Ce^{3+}	0.000	0.002	0.000	0.000	0.001
Al_2O_3	0.00	0.00	0.13	0.00	0.00	Pr^{3+}	0.001	0.000	0.002	0.000	0.000
Y_2O_3	27.78	26.69	28.69	27.41	32.16	Nd^{3+}	0.000	0.002	0.001	0.000	0.005
La_2O_3	0.04	-	-	-	-	Sm^{3+}	0.001	0.005	0.000	0.000	0.005
Ce_2O_3	0.02	0.06	-	-	0.04	Eu^{3+}	0.002	0.001	0.001	0.001	0.001
Pr_2O_3	0.06	-	0.09	-	-	Gd^{3+}	0.053	0.054	0.051	0.045	0.086
Nd_2O_3	0.01	0.10	0.03	-	0.19	Tb^{3+}	0.000	0.002	0.000	0.000	0.004
Sm_2O_3	0.03	0.19	0.01	-	0.18	Dy^{3+}	0.071	0.065	0.064	0.053	0.101
Eu_2O_3	0.07	0.02	0.05	0.03	0.03	Ho^{3+}	0.013	0.007	0.008	0.008	0.009
Gd_2O_3	2.24	2.32	2.19	1.93	3.53	Er^{3+}	0.065	0.049	0.063	0.061	0.062
Tb_2O_3	0.00	0.10	-	-	0.19	Tm^{3+}	0.005	0.003	0.004	0.004	0.004
Dy_2O_3	3.09	2.90	2.82	2.32	4.24	Yb^{3+}	0.047	0.032	0.045	0.048	0.025
Ho_2O_3	0.58	0.30	0.35	0.38	0.37	Lu^{3+}	0.010	0.009	0.009	0.010	0.011
Er_2O_3	2.91	2.25	2.85	2.74	2.66	Ca^{2+}	0.711	0.791	0.765	0.733	0.468
Tm_2O_3	0.21	0.15	0.17	0.17	0.17	ΣA	2.032	2.016	2.098	1.991	2.043
Yb_2O_3	2.19	1.52	2.07	2.22	1.13	Ti^{4+}	0.008	0.011	0.009	0.014	0.001
Lu_2O_3	0.46	0.41	0.44	0.46	0.50	Fe^{2+}	0.465	0.419	0.396	0.369	0.427
BeO*	8.22	7.62	9.18	7.50	9.41	Mn^{2+}	0.002	0.006	0.002	0.003	0.001
FeO	7.84	7.17	6.69	6.27	6.92	Mg^{2+}	0.003	0.003	0.000	0.000	0.000
MgO	0.03	0.03	-	-	-	Al^{3+}	0.000	0.000	0.011	0.000	0.000
MnO	0.04	0.11	0.04	0.05	0.01	□	0.522	0.561	0.581	0.614	0.572
CaO	9.35	10.56	10.08	9.72	5.93	ΣM	1.000	1.000	1.000	1.000	1.000
F	-	-	0.04	-	-	B^{3+}*	0.597	0.720	0.438	0.731	0.334
F=O	-	-	–0.02	-	-	Be^{2+}*	1.403	1.280	1.562	1.269	1.666
H_2O**	2.20	2.40	2.46	2.61	2.33	ΣQ	2.000	2.000	2.000	2.000	2.000
Total	100.69	99.69	100.52	98.61	99.86	$Si^{4+}=\Sigma T$	2.000	2.000	2.000	2.000	2.000
ΣREE_2O_3	39.68	37.00	39.76	37.66	45.38	O^{2-}	0.957	0.878	0.837	0.772	0.857
$\Sigma(Th,U)O_2$	0.15	0.06	0.16	0.10	0.08	OH^-**	1.043	1.122	1.163	1.228	1.143
						F^-	0.000	0.000	0.000	0.000	0.000
						$\Sigma\varphi$	2.000	2.000	2.000	2.000	2.000

*B_2O_3 and BeO contents calculated from charge balance, **H_2O content calculated on the basis of ideal stoichiometry. - = not analysed/calculated. 0.00 wt.% values indicate below the detection limit.

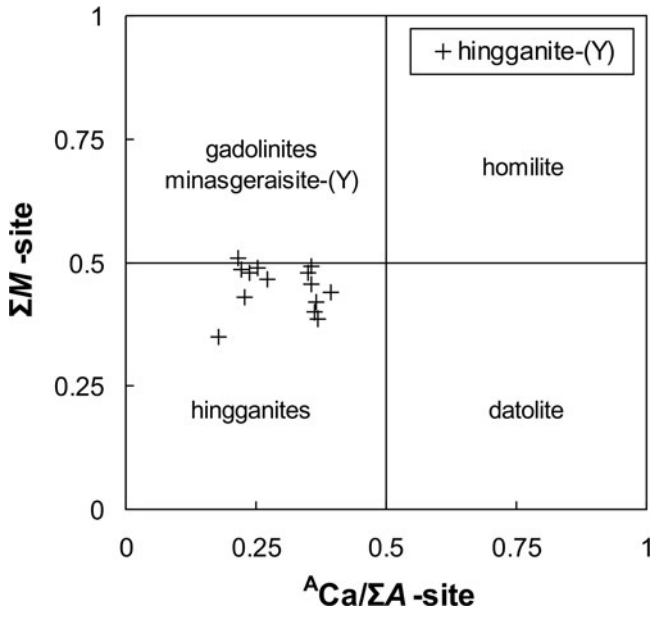

Fig. 7. Classification diagram of the gadolinite-group minerals from Bačík *et al.* (2017) with the positions of hingganite-(Y) from the Fabova Hoľa metagranite.

NYF (Nb–Y–F) granitic pegmatites (Hogarth *et al.*, 1972; Mellini and Merlino, 1977; Ma *et al.*, 1986; Miyawaki *et al.*, 1987, 2015; Pieczka *et al.*, 2015) and in the Predazzo granite, Italy (Emiliani and Gandolfi, 1965; Mellini and Merlino, 1977). In contrast, its occurrence, which has been documented in a late greenschist-facies regional metamorphic assemblage in the form of micro-veins transecting chloritite rock from the Abitibi greenstone belt, Ontario and Quebec, Canada, indicates that Y and B were mobilised during the low-grade metamorphism (Pan *et al.*, 1994). Other members of hellandite-group minerals [general chemical formula: $X_4Y_2ZT_2(B_4Si4O_{22})W_2$; Oberti *et al.* 2019] show a strong dominance of Ce over Y and LREE>HREE. They have also been described in alkaline rocks, mainly in miarolitic cavities and vugs of syenitic ejecta in volcanic rocks from Latium, Italy [hellandite-(Ce), mottanaite-(Ce) $Ca_4Ce_2Al(Be_{1.5}□_{0.5})(B_4Si_4O_{22})O_2$, ferri-mottanaite-(Ce) $Ca_4Ce_2Fe^{3+}(Be_{1.5}□_{0.5})(B_4Si_4O_{22})O_2$, ciprianiite $Ca_4(ThCa)Al(Be_{1.5}□_{0.5})(B_4Si_4O_{22})O_2$; Della Ventura *et al.*, 1999, 2002; Oberti *et al.*, 1999, 2019; Perna *et al.*, 2021] or in metasomatic rocks associated with alkaline magmatic rocks from the Dara-i-Pioz complex, Tajikistan, and the Hodza-Achkan massif, Kyrgyzstan [tadzhikite-(Ce) $Ca_4Ce_2Ti□_2(B_4Si_4O_{22})O_2$; Reguir *et al.*, 1999; Pautov *et al.*, 2013]. Mottanaite-(Ce), ferri-mottanaite-(Ce), ciprianiite and some hellandite-(Ce) also contain a notable concentration of Be (1.8–3.0 wt.% BeO; 0.7–1.2 apfu; Della Ventura *et al.*, 2002; Oberti *et al.*, 2019; Perna *et al.*, 2021), which occupies a special tetrahedral *T* site, usually vacant in hellandite-(Y), hellandite-(Ce) and tadzhikite-(Ce) (e.g. Oberti *et al.*, 2002, 2019).

https://doi.org/10.1180/mgm.2022.7 Published online by Cambridge University Press

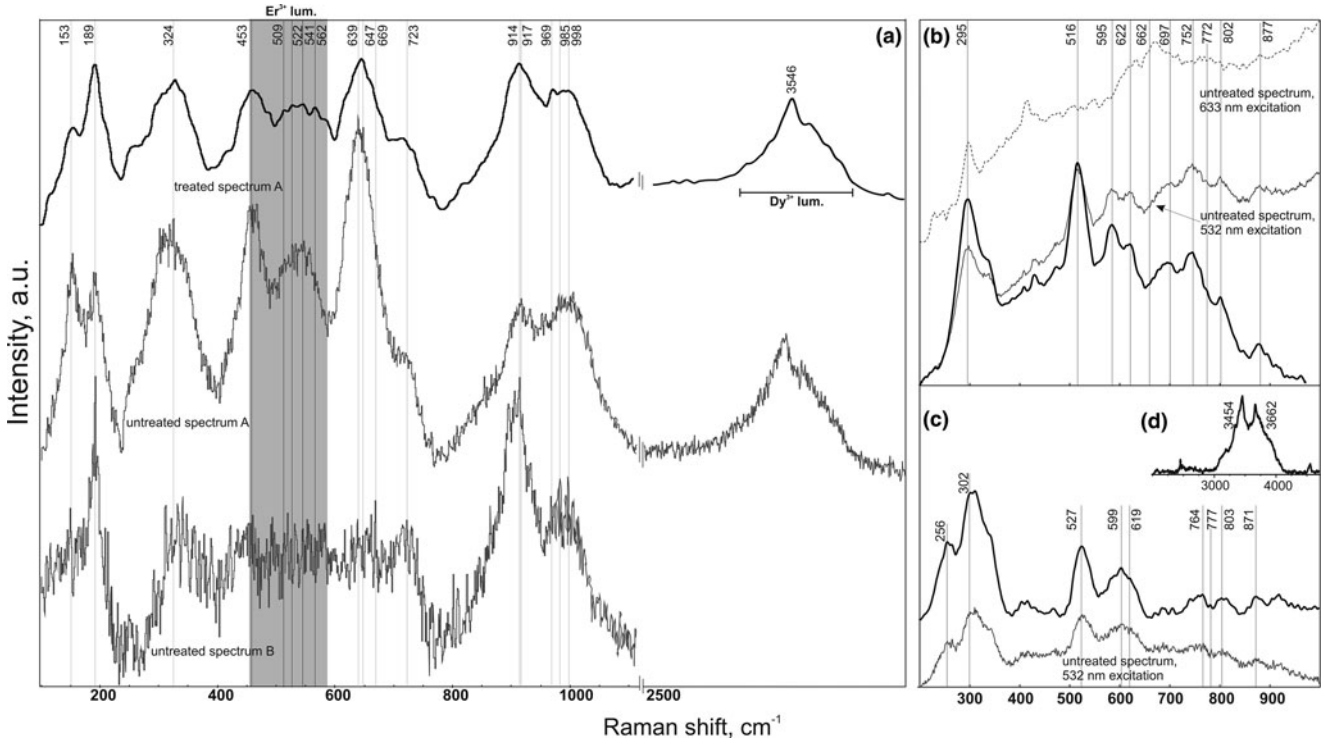

Fig. 8. (a) Raman spectra of hingganite-(Y) excited by a 532 nm laser; two different orientations of the crystal (A and B). (b, c, d) Raman spectra of hellandite-(Y) excited by a 532 nm laser for two different crystals and spectrum of hellandite-(Y) excited by a 633 nm laser (dashed line).

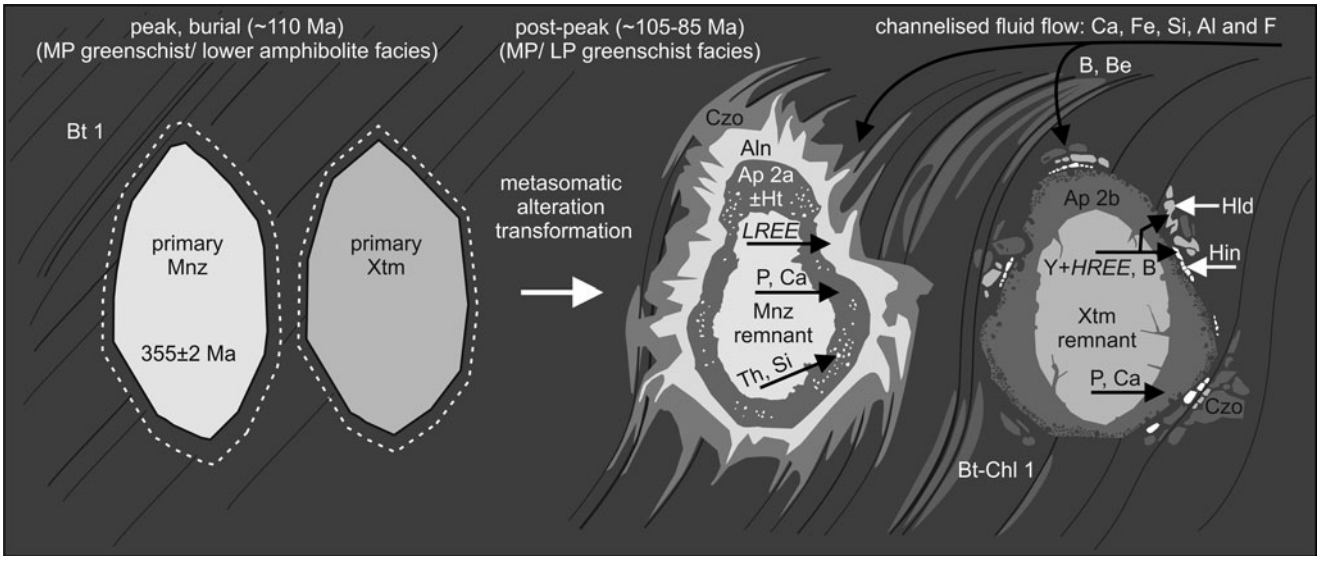

Fig. 9. Summary sketch of the main stages of monazite/ xenotime metasomatic alteration transformation.

The crucial factors in controlling the competitive crystallisation of hellandite-(Y) or hingganite-(Y) are most probably the local Al–Fe redistribution and the Fe^{2+}/Fe^{3+} ratio; where hellandite-(Y) contains a significant Al content and only minor amounts of Fe^{3+} (cf. Pan *et al.*, 1994), whereas the gadolinite–hingganite series is Al-free and favours Fe^{2+} instead of Fe^{3+} (Tables 3 and 4) (cf. Miyawaki *et al.*, 1984; Demartin *et al.*, 1993, 2001b; Cámara *et al.*, 2008; Bačík *et al.*, 2014). Extremely rare ferri-mottanaite-(Ce), the first Fe^{3+}-dominant hellandite group mineral from the Vico volcanic province, Italy (Oberti *et al.*, 2019), and ferri-hellandite-(Ce) $[(Ca_3Ce)Ce_2Fe^{3+}\square_2Si_4B_4O_{22}(OH)_2]$ from the Sagåsen larvikite quarry, Mørje, Porsgrunn, Vestfold and Telemark, Norway (Friis *et al.*, 2021), were described only recently. Nevertheless, a second important factor could prevent the crystallisation of Fe^{3+}-rich hellandite-group minerals; namely the local Be:B ratio. Amounts of Be could rise to give a ratio of 1.5:4 in the hellandite group (Oberti *et al.*, 2019; Della Ventura *et al.*, 2002), and more than 1:1 in the gadolinite-group minerals (Bačík *et al.*, 2017). Our data on hellandite-(Y) do not exclude the presence of Be – some of the Raman bands at 810–790 cm^{-1} and

https://doi.org/10.1180/mgm.2022.7 Published online by Cambridge University Press

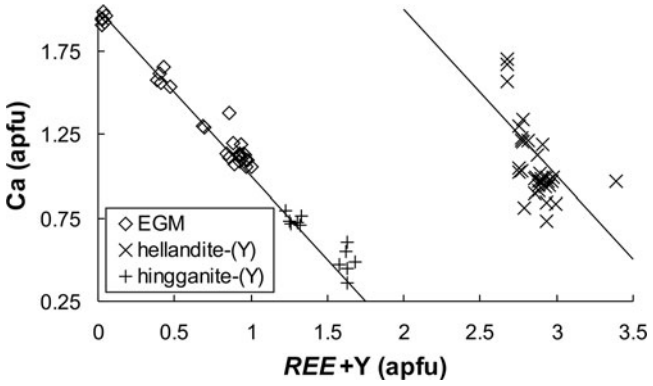

Fig. 10. Composition of secondary (boro)silicates in REE+Y vs. total Ca substitution diagram (atomic proportions) with ideal Ca:REE+Y substitution vectors (straight lines). Note: the REE+Y content in hellandite-(Y) is restricted to the *X* site only.

770–768 cm^{-1} could be attributed not only to Si–O but also Be–O stretching vibrations. However, the presence of sharp O–H peaks at 3454 and 3662 cm^{-1} indicate a significant proportion of OH^- groups in the *T* site cavity. Therefore, we can assume that the possible Be (or Li) occupancy at the *T* site of hellandite-(Y) is very probably limited, however without accurate measurement, this limit cannot be quantified. Consequently, if the Be:B ratio significantly exceeds 1:1 in the environment, hingganite-(Y) preferentially crystallises and binds Be, Fe^{2+}, and also a small amount of remaining B.

Although allanite-(Ce) and LREE-rich epidote are typical reaction products which accumulate LREE during monazite-(Ce) alteration in common granitic and metapelitic rocks over a wide *P–T* range, the analogous replacement of xenotime-(Y) produces only a limited amount of allanite-(Y), HREE+Y-rich epidote, and a significant amount of HREE+Y can be accommodated by apatite-supergroup minerals (cf. Broska *et al.*, 2005; Budzyń *et al.*, 2017; Hentschel *et al.*, 2020). Moreover, allanite-(Y) and epidote-group minerals, rich in HREE+Y, are very rare in nature and occur mainly in highly evolved felsic rocks, e.g. granitic pegmatites, rare-metal (leuco)granites, and associated metamorphic REE mineralisation veins (e.g. Gieré and Sorensen, 2004; Alekseev *et al.*, 2013, 2016). These data, together with our observations, raise a question regarding the relative stability between LREE-rich epidote-group minerals and HREE+Y-rich epidote-group minerals in magmatic and metamorphic systems, and suggest that the HREE and Y mainly reside in other minerals (Gieré and Sorensen, 2004). A possible explanation for this disparity in the Fabova Hoľa granite samples is a higher B activity during mylonitisation (~15–20 ppm B in the metagranite; Marsina *et al.*, 1999), which favours the formation of borosilicates instead of epidote-group minerals. A similar scenario for hydrothermal tourmalinisation, and its influence on LREE vs. HREE accumulation and allanite formation was proposed by Balashov (1976) and later by Alekseev *et al.* (2016) regarding allanite-(Ce) and allanite-(Y) paragenesis in a tourmalinite from the Severnyi pluton, Chukchi Peninsula, Russia. The stability of LREE-rich epidote-group minerals vs. HREE+Y-rich gadolinite-group minerals and the HREE +Y-rich (boro)silicate alternatives are also evident in the Strange Lake peralkaline pluton in Canada, where LREE mobility was controlled largely by the stability of ferriallanite-(Ce), whereas HREE was controlled by gadolinite-(Y) (Gysi *et al.*, 2016; Vasyukova and William-Jones, 2019). However, little is currently known regarding the formation of HREE+Y-rich epidote-group minerals vs. HREE +Y-rich gadolinite-group minerals during alteration of natural xenotime-(Y). Moreover, though a few experiments have focused on the relative stabilities of xenotime-(Y)–HREE+Y-rich epidote–HREE+Y-rich fluorapatite in high Ca and Na–Ca environments under different *P–T* conditions (e.g. Budzyń *et al.*, 2017), none have considered a B-(Be) saturated environment.

Crystal-chemical data for secondary (boro)silicates indicate solid solutions with a general Ca–REE+Y substitution trend (Fig. 10). This suggests that a major change in fluid chemistry occurred during hydrothermal alteration of monazite-(Ce) and xenotime-(Y), which was substantially controlled by the activity of Ca. Moreover, the remobilisation and distribution of LREE vs. HREE+Y was controlled by the competition between hydrothermal fluids and the stability of primary REE phosphates, as well as by the stability of secondary LREE epidote-group minerals and HREE+Y gadolinite-group minerals (cf. Gysi *et al.*, 2016). Formation of hellandite-(Y) and hingganite-(Y) in the Fabova Hoľa metagranite may have resulted from localised heterogeneity and a Y–B–Be saturated environment occurring in the proximity of the altered xenotime-(Y), instead of the more common accessory epidote-group minerals or tourmaline. This has been documented in metagranites in the broader vicinity of the FAH-3 sample (Dubík 1991; Putiš 1994). Hingganite-(Y) would have crystallised from Y–Be–B-rich fluids in the same manner.

Age of primary monazite-(Ce), formation of coronae as a function of P–T conditions, and the relationship to Alpine mylonitisation

An age of 355 ± 1.9 Ma obtained by *in situ* Th–U–total Pb EPMA of primary magmatic monazite-(Ce) are consistent with the SIMS zircon U–Pb radiometric age determination of the corresponding I-type granitic rocks from the Tatric and Veporic units (~350–360 Ma; Broska *et al.*, 2013), including the Sihla type tonalite dated to ca. 355 Ma directly from the Vepor pluton (Kohút *et al.*, 2008). It represents a primary magmatic age for emplacement of the granite during the main stage of Variscan plutonic activity in the West-Carpathian Tatric and Veporic crystalline basement (Poller *et al.*, 2000; Gaab *et al.*, 2005; Burda and Gawęda 2009; Kohút *et al.*, 2008; Broska *et al.*, 2013; Burda *et al.*, 2013a, 2013b; Gawęda *et al.*, 2016; Kohút and Larionov, 2021).

Determining the age from analysis of marginal parts of the monazite-(Ce) grains and isolated tiny monazite-(Ce) relics resulted in a scatter of younger ages (300 to 90 Ma). This less precise age interval indicates a disturbance in Th–U–Pb abundances, which was probably induced during alteration and coronae formation around monazite-(Ce) that resulted in partial-to-total Pb removal and partial resetting of the geochronometer (cf. Harlov *et al.*, 2011; Williams *et al.*, 2011).

The exhumation of mylonitised metagranites of the Fabova Hoľa Complex at ca. 90–85 Ma was constrained by ^{40}Ar–^{39}Ar phengite ages from the extensional shear zones (Putiš, 1994; Dallmeyer *et al.*, 1996; Putiš *et al.*, 2009a). The Late Cretaceous to Palaeocene uplift of the Veporic Unit is also documented by the zircon fission track age of the Sihla tonalite (64.9 ± 4.8 Ma; Plašienka *et al.*, 2007). Deformation here terminated in a brittle–ductile regime, and the opened 'en-echelon' or 'pinch and swell structures' are still infilled by late- to post-metamorphic mineralisation. The greenschist-facies tectono-metamorphic conditions during the metagranite exhumation and blastomylonitisation may

https://doi.org/10.1180/mgm.2022.7 Published online by Cambridge University Press

alternatively constrain the conditions of coronae formation (Putiš, 1994; Putiš *et al.*, 1997b; Janák *et al.*, 2001; Lupták *et al.*, 2000; Jeřábek *et al.*, 2007, 2008a, 2008b). The coronae-bearing domains could be indicators of a channelised fluid flow during the exhumation. These domains are always located in a granitic blastomylonitic groundmass composed of newly formed medium-pressure greenschist-facies minerals, such as quartz-2, albite, chlorite, phengite, biotite-2, epidote, clinozoisite, ±grossular-rich garnet and calcite. Therefore, the estimated *P–T* conditions of corona formation are from ca. 450 to 300°C following the exhumation ductile deformation regime and still a high late-metamorphic fluid activity. The outer rims of coronae are frequently ingrowing the hosting deformed biotite-1, being partly altered to phengite and chlorite (Fig. 9). Similarly, the brittle fractures of the neighbouring semiductile feldspars are infilled by quartz, albite and chlorite.

Possible sources of B and Be

The presence of hellandite-(Y) and hingganite-(Y) in the coronae mineral aggregates requires a source of B and Be, which could have been remobilised during fluid-mediated breakdown of xenotime-(Y). Two principal sources of B and Be could be: (1) internal origin from rock-forming or accessory minerals of the host metagranite; or (2) resulting from external sources such as adjacent magmatic, metamorphic and sedimentary rocks.

The B content in common plutonic and metamorphic plagioclase and K-feldspar can usually be up to 100 ppm B, which could be incorporated as the $(Na,K)BSi_3O_8$ molecule in the feldspars. Boron could have been leaked into the circulating fluid during the post-magmatic orthoclase to microcline ordering of K-feldspar (Grew, 2002a). Plagioclase is a principal source of B in common tourmaline-free granites. It contributes up to 69 wt.% of the whole B content in the rock (Sauerer and Troll, 1990). The mica-group minerals, especially muscovite, also represent an important carrier of B among granitic rock-forming minerals, where B substitutes for Al in the tetrahedral site as a boromuscovite molecule (Grew, 2002a). The concentration of Be in rock-forming minerals of common two-mica granites is generally very low, usually ≤10 ppm (Kretz *et al.*, 1989).

Alternatively, or even additionally, the potential *in situ* source of B could be the altered xenotime-(Y) itself. The xenotime contains traces of B, which has been documented by X-ray compositional mapping (Fig. 5i). The incorporation of B into the xenotime-(Y) structure is most probably controlled by coupled heterovalent substitution $(Nb,Ta)BY_{-1}P_{-1}$ (Nb^{5+}, $Ta^{5+} + B^{3+} \leftrightarrow Y^{3+} + P^{5+}$), though in a limited range due to a very low Nb content, (close to the detection limit) in the xenotime-(Y). The natural occurrences of schiavinatoite ($NbBO_4$) and béhierite ($TaBO_4$), together with the Nb–Ta orthoborates with a zircon–xenotime type crystal structure (Mrose and Rose, 1962; Range *et al.*, 1996; Demartin *et al.*, 2001a; Finch and Hanchar, 2003), together with previous indications of B replacing P in xenotime-(Y) (Oftendal, 1964), support the presence of B in the xenotime-(Y) and the existence of a possible limited xenotime-(Y)–schiavinatoite–béhierite solid solution as a source of B.

The second possibility represents an external source of B and Be during the Alpine tectono-thermal overprint of the Fabova Hoľa metagranites The B-bearing environment, necessary for hellandite-(Y) and hingganite-(Y) formation, is supported by the occurrence of abundant newly formed tourmaline neoblasts in the adjacent Variscan Veporic metatonalites and tourmalinite pebbles in the Permian basal conglomerates (Vozárová *et al.*, 2016), as well as in the surrounding Palaeozoic micaceous metapelites (cf. Lupták *et al.*, 2000; Janák *et al.*, 2001; Jeřábek *et al.*, 2008b). Schorlitic tourmaline is a mineral commonly found in the Permian Klenovec-type granite, which occurs as several small intrusions in the Veporic Unit (Hraško *et al.*, 2002; Villaseñor *et al.*, 2021).

Consequently, B and Be could have been mobilised during Alpine mylonitisation, and in the associated tectono-thermal fluid that overprinted the *in situ* rock-forming minerals, especially muscovite and feldspars. These are the principal host phases for B and also Be, considering their high modal abundance in the parental granitic rocks (cf. Domanik *et al.*, 1993; Leeman and Sisson, 1996; London *et al.*, 1996; Grew, 2002a, 2002b; and references therein).

Acknowledgements. This work is dedicated to the memory of Jarmila Luptáková, PhD, who sadly passed away aged 45 on Sunday 27th June, 2021. This work was supported by the Slovak Research and Development Agency under contracts APVV–15–0050, APVV–18–0065, APVV–19–0065, and VEGA Agency Nos. 1/0467/20 and 1/0151/19. We thank P. Konečný and V. Kollárová for providing the EPMA facilities, as well as Michael J. Sabo for reviewing the English content. Finally, we thank Daniel Harlov, Fernando Cámara, one anonymous reviewer and Roger Mitchell (Principal Editor) for their constructive suggestions.

Supplementary material. To view supplementary material for this article, please visit https://doi.org/10.1017/S0007123422000011

References

Alekseev V.I., Marin Yu.B. and Gembitskaya I.M. (2013) Allanite-(Y) in areas of ongonite magmatism in the Far East: Isomorphism and petrogenetic implications. *Geology of Ore Deposits*, **55**, 503–514.

Alekseev V.I., Marin Yu.B. and Gembitskaya I.M. (2016) Allanite-(Y) and allanite-(Ce) paragenesis in tourmalinite of the Severnyi pluton, Chukchi Peninsula and the relationship between yttrium and lanthanides in allanite. *Geology of Ore Deposits*, **58**, 674–680.

Åmli R. and Griffin W. (1975) Microprobe analysis of REE minerals using empirical correction factors. *American Mineralogist*, **60**, 599–606.

Armbruster T., Bonazzi P., Akasaka M., Bermanec V., Chopin C., Gieré R., Heuss-Assbichler S., Liebscher A., Menchetti S., Pan Y. and Pasero M. (2006) Recommended nomenclature of epidote-group minerals. *European Journal of Mineralogy*, **18**, 551–567.

Bačík P., Fridrichová J., Uher P., Pršek J. and Ondrejka M. (2014) Crystal chemistry of gadolinite-datolite group silicates. *The Canadian Mineralogist*, **51**, 625–642.

Bačík P., Miyawaki R., Atencio D., Cámara F. and Fridrichová J. (2017) Nomenclature of the gadolinite supergroup. *European Journal of Mineralogy*, **29**, 1067–1082.

Balashov Yu.A. (1976) *Geochemistry of the Rare-Earth Elements*. Nauka, Moscow [in Russian].

Barrat J.A., Zanda B., Moynier F., Bollinger C., Liorzou C. and Bayon G. (2012) Geochemistry of CI chondrites: Major and trace elements, and Cu and Zn Isotopes. *Geochimica et Cosmochimica Acta*, **83**, 79–92.

Bea, F. (1996) Residence of REE, Y, Th and U in granites and crustal protoliths; implications for the chemistry of crustal melts, *Journal of Petrology*, **37**, 521–552.

Berger A., Gnos E., Janots E., Fernandez A. and Giese J. (2008) Formation and composition of rhabdophane, bastnäsite and hydrated thorium minerals during alteration: Implications for geochronology and low-temperature processes. *Chemical Geology*, **254**, 238–248.

Bezák V. (1994) Proposal of the new division of the West Carpathian crystalline based on the Hercynian tectonic building reconstruction. *Mineralia Slovaca*, **26**, 1–6 [in Slovak with English summary].

Biely A., Bezák V., Elečko M., Kaličiak M., Konečný V., Lexa J., Mello J., Nemčok J., Potfaj M., Rakús M., Vass D., Vozár J. and Vozárová A.

(1996) *Geological Map of Slovakia 1:500000*. State Geological Institute of Dionýz Štúr, Bratislava, Slovakia.

Bodył S., Czaja M. and Mazurak Z. (2009) Optical properties of Pr^{3+}, Sm^{3+} and Er^{3+} ions in apatite, fluorite and phosphate glasses. *Physics Procedia*, **2**, 515–525

Broska I. and Petrík I. (2015) Variscan thrusting in I- and S-type granitic rocks of the Tribeč Mountains, Western Carpathians (Slovakia): evidence from mineral compositions and monazite dating. *Geologica Carpathica*, **66**, 455–471.

Broska I. and Siman P. (1998) The breakdown of monazite in the West-Carpathian Veporic orthogneisses and Tatric granites. *Geologica Carpathica*, **49**, 161–167.

Broska I. and Uher P. (2001) Whole-rock chemistry and genetic typology of the West-Carpathian Variscan granites. *Geologica Carpathica*, **52**, 79–90.

Broska I., Williams C.T., Uher P., Konečný P. and Leichmann J. (2004) The geochemistry of phosphorus in different granite suites of the Western Carpathians, Slovakia: the role of apatite and P-bearing feldspar. *Chemical Geology*, **205**, 1–15.

Broska I., Williams C.T., Janák M. and Nagy G. (2005) Alteration and breakdown of xenotime-(Y) and monazite-(Ce) in granitic rocks of the Western Carpathians, Slovakia. *Lithos*, **82**, 71–83.

Broska I., Petrík I., Be´eri-Shlevin Y., Majka J. and Bezák V. (2013) Devonian/Mississippian I-type granitoids in the Western Carpathians: A subduction-related hybrid magmatism. *Lithos*, **162–163**, 27–36.

Budzyń B. and Kozub-Budzyń G.A. (2015) The stability of xenotime in high Ca and Ca-Na systems, under experimental conditions of 250–350°C and 200–400 MPa: the implications for fluid-mediated low-temperature processes in granitic rocks. *Geological Quarterly*, **59**, 316–324.

Budzyń B., Hetherington C.J., Williams M.L., Jercinovic M.J. and Michalik M. (2010) Fluid–mineral interactions and constraints on monazite alteration during metamorphism. *Mineralogical Magazine*, **74**, 659–681.

Budzyń B., Harlov D., Williams M.L. and Jercinovic M.J. (2011) Experimental determination of stability relations between monazite, fluorapatite, allanite, and REE-epidote as a function of pressure, temperature, and fluid composition. *American Mineralogist*, **96**, 1547–1567.

Budzyń B., Harlov D.E., Kozub-Budzyń G.A. and Majka J. (2017) Experimental constraints on the relative stabilities of the two systems monazite-(Ce) – allanite-(Ce) – fluorapatite and xenotime-(Y) – (Y, HREE)-rich epidote – (Y,HREE)-rich fluorapatite, in high Ca and Na-Ca environments under P-T conditions of 200–1000 MPa and 450–750 °C. *Mineralogy and Petrology*, **111**, 183–217.

Budzyń B., Sláma J., Kozub-Budzyń G.A., Konečný P., Holický I., Rzepa G. and Jastrzębski M. (2018) Constraints on the timing of multiple thermal events and re-equilibration recorded by high-U zircon and xenotime: Case study of pegmatite from Piława Górna (Góry Sowie Block, SW Poland). *Lithos*, **310–311**, 65–85.

Burda J. and Gawęda A. (2009) Shear-influenced partial melting in the Western Tatra metamorphic complex: geochemistry and geochronology. *Lithos* **110**, 373–385.

Burda J., Gawęda A. and Klötzli U. (2013a) Geochronology and petrogenesis of granitoid rocks from the Goryczkowa Unit, Tatra Mountains (Central Western Carpathians). *Geologica Carpathica* **64**, 419–435.

Burda J., Gawęda A. and Klötzli U. (2013b) U–Pb zircon age of the youngest magmatic activity in the High Tatra granites (Central Western Carpathians). *Geochronometria*, **40**, 134–144.

Cámara F., Oberti R., Ottolini L., Della Ventura G. and Bellatreccia F. (2008) The crystal chemistry of Li in gadolinite. *American Mineralogist*, **93**, 996–1004.

Dallmeyer R.D., Neubauer F. and Putiš M. (1993) $^{40}Ar/^{39}Ar$ mineral age controls for the Pre-Alpine and Alpine tectonic evolution of nappe complexes in the Western Carpathians. *PAEWCR Conference, Excursion guide, Stará Lesná, Slovakia*, 11–20.

Dallmeyer R.D., Neubauer F., Handler R., Fritz H., Müller W., Pana D. and Putiš M. (1996) Tectonothermal evolution of the internal Alps and Carpathians: Evidence from $^{40}Ar/^{39}Ar$ mineral and whole-rock data. *Eclogae Geologicae Helvetiae*, **89**, 203–227.

de Bettencourt-Dias A. (2014) *Luminescence of Lanthanide Ions in Coordination Compounds and Nanomaterials*. Wiley, Chichester, England.

Della Ventura G., Williams C.T., Cabella R., Oberti R., Caprilli E. and Bellatreccia F. (1999) Britholite-hellandite intergrowths and associated REE-minerals from the alkali-syenitic ejecta of the Vico volcanic complex (Latium, Italy): petrological implications bearing on REE mobility in volcanic systems. *European Journal of Mineralogy*, **11**, 843–854.

Della Ventura G., Bonazzi P., Oberti R. and Ottolini L. (2002) Ciprianiite and mottanaite-(Ce), two new minerals of the hellandite group from Latium (Italy). *American Mineralogist*, **87**, 739–744.

Demartin F., Pilati T., Diella V., Gentile P. and Gramaccioli C.M. (1993) A crystal-chemical investigation of Alpine gadolinite. *The Canadian Mineralogist*, **30**, 127–136.

Demartin F., Diella V., Gramaccioli C.M. and Pezzotta F. (2001a) Schiavinatoite, $(Nb,Ta)BO_4$, the Nb analogue of behierite. *European Journal of Mineralogy*, **13**, 159–165.

Demartin F., Minaglia A. and Gramaccioli C.M. (2001b) Characterization of gadolinite-group minerals using crystallographic data only: the case of hingganite-(Y) from Cuasso al Monte, Italy. *The Canadian Mineralogist*, **39**, 1105–1114.

Domanik K.J., Hervig R.L. and Peacock S.M. (1993) Beryllium and boron in subduction zone minerals: An ion microprobe study. *Geochimica et Cosmochimica Acta*, **57**, 4997–5010.

Dubík B. (1991) *Structural and petrological aspects of the Fabova Hoľa massif in the Veporic Unit*. MSc thesis, unpublished. Bratislava [in Slovak].

Emiliani F. and Gandolfi G. (1965) The accessory minerals from Predazzo granite (North Italy). Part III (datolite, gadolinite, hellandite, ancylite, synchisite, uraninite). *Mineralogica Petrografica Acta*, **11**, 123–131.

Engi M. (2017) Petrochronology based on REE-minerals: monazite, allanite, xenotime, apatite. Pp 365–418 in: *Petrochronology: Methods and Applications* (M.J. Kohn, M. Engi and P. Lanari, editors). Reviews in Mineralogy and Geochemistry, **83**, Mineralogical Society of America, Chantilly, Virginia, USA.

Finch R.J. and Hanchar J.M. (2003) Structure and chemistry of zircon and zircon-group minerals. Pp. 1–25 in: *Zircon* (J.M. Hanchar and P.W.O. Hoskin, editors). Reviews in Mineralogy and Geochemistry, **53**, Mineralogical Society of America, Chantilly, Virginia, USA.

Finger F., Broska I., Roberts M. and Schermaier A. (1998) Replacement of primary monazite by apatite–allanite–epidote coronas in an amphibolite facies granite gneiss from the eastern Alps. *American Mineralogist*, **85**, 248–258.

Finger F., Krenn E., Schulz B., Harlov D. and Schiller D. (2016) "Satellite monazites" in polymetamorphic basement rocks of the Alps: Their origin and petrological significance. *American Mineralogist*, **101**, 1094–1103.

Förster H.-J. (1998a) The chemical composition of REE-Y-Th-U-rich minerals in peraluminous accessory granites of the Erzgebirge-Fichtelgebirge region, Germany. Part I: The monazite-(Ce)-brabantite solid solution series. *American Mineralogist*, **83**, 259–272.

Förster H.-J. (1998b) The chemical composition of REE-Y-Th-U-rich minerals in peraluminous accessory granites of the Erzgebirge-Fichtelgebirge region, Germany. Part II: Xenotime. *American Mineralogist*, **83**, 1302–1315.

Friis H., Škoda R., Larsen A.O., Vašinová-Galiová M., Čtvrtlík R. and Filip J. (2021) Ferri-hellandite-(Ce), IMA 2020–085. CNMNC Newsletter 60; *Mineralogical Magazine*, **85**, 454–458.

Frost R.L., Xi Y., Scholz R., Lima R.M.F., Horta L.F.C. and Lopez A. (2013) Thermal analysis and vibrational spectroscopic characterization of the boro silicate mineral datolite – $CaBSiO_4(OH)$. *Spectrochimica Acta*, **A115**, 376–381

Gaab A.S., Poller U., Janák M., Kohút M. and Todt W. (2005) Zircon U-Pb geochronology and isotopic characterization for the pre-Mesozoic basement of the Northern Veporic Unit (Central Western Carpathians, Slovakia). *Schweizerische Mineralogische und Petrographische Mitteilungen*, **85**, 69–88.

Gaft M., Reisfeld R. and Panczer G. (2005) *Modern Luminescence Spectroscopy of Minerals and Materials*. Pp 356, Springer-Verlag Berlin Heidelberg.

Gawęda A., Burda J., Klötzli U., Golonka J. and Szopa K. (2016) Episodic construction of the Tatra granitoid intrusion (Central Western Carpathians, Poland/Slovakia): consequences for the geodynamics of Variscan collision and Rheic Ocean closure. *International Journal of Earth Sciences* **105**, 1153–1174.

Gieré R. and Sorensen S.S. (2004) Allanite and other REE-rich epidote-group minerals. Pp. 431–493 in: *Epidotes* (A. Liebscher and G. Franz, editors). Reviews in Mineralogy and Geochemistry, **56**, Mineralogical Society of America, Chantilly, Virginia, USA.

https://doi.org/10.1180/mgm.2022.7 Published online by Cambridge University Press

Gorelova L., Vereshchagin O., Cuchet S., Shilovskikh V. and Pankin D. (2020) Low-temperature crystal chemistry of hingganite-(Y), from the Wanni Glacier, Switzerland. *Minerals,* **10**, 322.

Goryainov S.V., Krylov A.S., Vtyurin A.N. and Pan Y. (2015) Raman study of datolite $CaBSiO_4(OH)$ at simultaneously high pressure and high temperature. *Journal of Raman Spectroscopy*. **46**, 177–181.

Gratz R. and Heinrich W. (1997) Monazite-xenotime thermobarometry: experimental calibration of the miscibility gap in the binary system $CePO_4$-YPO_4. *American Mineralogist*, **82**, 772–780.

Grew E.S. (2002a) Borosilicates (exclusive of tourmaline) and boron in rock-forming minerals in metamorphic environment. Pp 387–502 in: *Boron: Mineralogy, Petrology and Geochemistry* (E.S. Grew and L.M. Anowitz, editors) Reviews in Mineralogy, **33**, Second printing with corrections and additions. Mineralogical Society of America, Washington, DC, USA.

Grew E.S. (2002b) Beryllium in metamorphic environments (emphasis on aluminous compositions). Pp 487–549 in: *Beryllium: Mineralogy, Petrology and Geochemistry* (E.S. Grew, editor) Reviews in Mineralogy and Geochemistry, 50. Mineralogical Society of America, Washington, DC, USA.

Gysi A.P., Williams-Jones A.E. and Collins P. (2016) Lithogeochemical vectors for hydrothermal processes in the Strange lake peralkaline granitic REE-Zr-Nb deposit. *Economic Geology*, **111**, 1241–1276.

Harlov D.E. and Wirth R. (2012) Experimental incorporation of Th into xenotime at middle to lower crustal P-T utilizing alkali-bearing fluids. *American Mineralogist*, **97**, 641–652.

Harlov D.E., Wirth R. and Hetherington C.J. (2011) Fluid-mediated partial alteration in monazite: the role of coupled dissolution–reprecipitation in element redistribution and mass transfer. *Contributions to Mineralogy and Petrology*, **162**, 329–348.

Heinrich W., Andrehs G. and Franz G. (1997) Monazite-xenotime miscibility gap thermometry. I. An empirical calibration. *Journal of Metamorphic Geology*, **15**, 3–16.

Hentschel F., Janots E., Trepmann C.A., Magnin V. and Lanari P. (2020) Corona formation around monazite and xenotime during greenschist-facies metamorphism and deformation. *European Journal of Mineralogy*, **32**, 521–544.

Hetherington C.J. and Harlov D.E. (2008) Metasomatic thorite and uraninite inclusions in xenotime and monazite from granitic pegmatites, Hidra anorthosite massif, southwestern Norway: Mechanics and fluid chemistry. *American Mineralogist*, **93**, 806–820.

Hetherington C.J., Harlov D.E. and Budzyń B. (2010) Experimental metasomatism of monazite and xenotime: mineral stability, REE mobility and fluid composition. *Mineralogy and Petrology*, **99**, 165–184.

Hofmeister A.M., Hoering T.C. and Virgo D. (1987) Vibrational spectroscopy of beryllium aluminosilicates: Heat capacity calculations from band assignments. *Physics and Chemistry of Minerals*, **14**, 205–224.

Hogarth D.D., Chao G.Y. and Harris D.C. (1972) New data on hellandite. *The Canadian Mineralogist*, **11**, 760–776.

Hraško Ľ., Broska I. and Finger F. (2002) Permian granitic magmatism and disintegration of the Lower Paleozoic basement in the SW veporicum near Klenovec (Western Carpathians). Pp. 7 in: *Proceedings of XVII. Congress of Carpathian–Balkan Geological Association* (J. Michalik, L. Šimon and J. Vozár, editors), Geologica Carpathica Special Issue **53**, Bratislava, Slovakia.

Janák M., Plašienka D., Frey M., Cosca M., Schmidt S.Th., Lupták B. and Méres Š. (2001) Cretaceous evolution of a metamorphic core complex, the Veporic unit, Western Carpathians (Slovakia): *P-T* conditions and *in situ* $^{40}Ar/^{39}Ar$ UV laser probe dating of metapelites. *Journal of Metamorphic Geology*, **19**, 197–216.

Janák M., Méres Š. and Ivan P. (2007). Petrology and metamorphic P-T conditions of eclogites from the northern Veporic unit, western Carpathians, Slovakia. *Geologica Carpathica*, **58**, 121–131.

Janots E., Engi M., Berger A., Allaz J., Schwartz J.-O. and Spandler C. (2008) Prograde metamorphic sequence of REE minerals in pelitic rocks of the Central Alps: implications for allanite–monazite–xenotime phase relations from 250 to 610 °C. *Journal of Metamorphic Geology*, **26**, 509–526.

Jeřábek P., Stünitz H., Heilbronner R., Lexa O. and Schulmann K. (2007) Microstructural–deformation record of an orogen-parallel extension in the Vepor Unit, West Carpathians. *Journal of Structural Geology*, **29**, 1722–1743.

Jeřábek P., Faryad S.W., Schulmann K., Lexa O. and Tajčmanová L. (2008a) Alpine burial and heterogeneous exhumation of Variscan crust in the West Carpathians: insight from thermodynamic and argon diffusion modelling. *Journal of the Geological Society*, **165**, 479–498.

Jeřábek P., Janák M., Faryad W., Finger F. and Konečný P. (2008b) Polymetamorphic evolution of pelitic schists and evidence for Permian low-pressure metamorphism in the Vepor Unit, West Carpathians. *Journal of Metamorphic Geology*, **26**, 465–485.

Ji L., Harlov D. and Wang F. (2021) Fluid-induced alteration of monazite, magnetite, and sulphides during the albitization of a Palaeoproterozoic granite from the Jiao-Liao-Ji orogenic belt, North China Craton. *Contributions to Mineralogy and Petrology*, **176**, 81.

Kohn M.J. and Malloy M.A. (2004) Formation of monazite via prograde metamorphic reactions among common silicates: implications for age determinations. *Geochimica et Cosmochimica Acta*, **68**, 101–113.

Kohút M. and Larionov A. (2021) From subduction to collision: Genesis of the Variscan granitic rocks from the Tatric Superunit (Western Carpathians, Slovakia). *Geologica Carpathica*, **72**, 96–113.

Kohút M., Uher P., Putiš M., Sergeev S. and Antonov A. (2008) Dating of the Lower Carboniferous granitic rocks from the Western Carpathians in the light of new SHRIMP U-Pb zircon data. *Mineralia Slovaca*, **40**, 204 [in Slovak].

Konečný V., Konečný P., Kubeš P. and Pécskay Z. (2015a) Paleovolcanic reconstruction of the Neogene Vepor stratovolcano (Central Slovakia), part I. *Mineralia Slovaca*, **47**, 1–76.

Konečný V., Konečný P., Kubeš P. and Pécskay Z. (2015b) Paleovolcanic reconstruction of the Neogene Vepor stratovolcano (Central Slovakia), part II. *Mineralia Slovaca*, **47**, 113–176.

Konečný P., Kusiak M.A. and Dunkley D.J. (2018) Improving U-Th-Pb electron microprobe dating using monazite age references. *Chemical Geology*, **484**, 22–35.

Kotov A.B., Miko O., Putiš M., Korikovsky S.P., Salnikova E.B., Kovach V.P., Yakovleva S.Z., Bereznaya N.G., Král' J. and Krist E. (1996) U/Pb dating of zircons of postorogenic acid metavolcanics and metasubvolcanics: A record of Permian-Triassic taphrogeny of the West-Carpathian basement. *Geologica Carpathica*, **47**, 73–79.

Kretz R., Loop J. and Hartree R. (1989) Petrology and Li–Be–B geochemistry of muscovite-biotite granite and associated pegmatite near Yellowknife, Canada. *Contributions to Mineralogy and Petrology*, **102**, 174–190.

Lafuente B., Downs R.T., Yang H. and Stone N. (2015) The power of databases: the RRUFF project. Pp. 1–30 in: *Highlights in Mineralogical Crystallography* (T. Armbruster and R.N. Danisi, editors). W. De Gruyter, Berlin, Germany.

Leeman W.P. and Sisson V.B. (1996) Geochemistry of boron and its implications for crustal and mantle processes. Pp 645–708 in: *Boron: Mineralogy, Petrology and Geochemistry* (E.S. Grew and L.M. Anovitz, editors) Reviews in Mineralogy and Geochemistry, **33**. Mineralogical Society of America, Washington, DC, USA.

Leite C.A.F., Guimarães R.B., Fernandes J.C., Continentino M.A., Paschoal C.W.A., Ayala A.P. and Guedes I. (2001) Temperature-dependent Raman scattering study of $Fe_3O_2BO_3$ ludwigite. *Journal of Raman Spectroscopy*, **33**, 1–5.

Lenz C., Nasdala L., Talla D., Hauzenberger C., Seitz R. and Kolitsch U. (2015) Laser-induced REE^{3+} photoluminescence of selected accessory minerals – An "advantageous artefact" in Raman spectroscopy. *Chemical Geology*, **415**, 1–16.

Lexa J., Seghedi I., Németh K., Szakács A., Konečný V., Pécskay Z., Fülöp A. and Kovacs M. (2010) Neogene-Quaternary Volcanic forms in the Carpathian-Pannonian Region: a review. *Central European Journal of Geosciences*, **2**, 207–270.

London D., Morgan VI G.B. and Wolf M.B. (1996) Boron in granitic rocks and their contact aureoles. Pp 299–330 in: *Boron: Mineralogy, Petrology and Geochemistry* (E.S. Grew and L.M. Anovitz, editors) Reviews in Mineralogy and Geochemistry, **33**. Mineralogical Society of America, Washington, DC, USA.

Lupták B., Janák M. and Plašienka D. (2000) Chloritoid-kyanite schists from the Veporic unit Western Charpathians Slovakia: implications for Alpine

https://doi.org/10.1180/mgm.2022.7 Published online by Cambridge University Press

(Cretaceous) metamorphism. *Schweizerische Mineralogische und Petrographische Mitteilungen*, **80**, 213–223.

Ma R., Zhang J. and Yang F. (1986) Hellandite of Quyang, in Hebei, China, *Acta Geologica Sinica*, **60**, 68–77 [Chinese with English abstract].

Majka J. and Budzyń B. (2006) Monazite breakdown in metapelites from Wedel Jarlsberg Land, Svalbard – preliminary report. *Mineralogia Polonica*, **37**, 61–69.

Majka J., Pršek J., Budzyń B., Bačík P., Barker A.K. and Łodziński M. (2011) Fluorapatite-hingganite-(Y) coronas as products of fluid-induced xenotime-(Y) breakdown in the Skoddefjellet pegmatite, Svalbard. *Mineralogical Magazine*, **75**, 159–167.

Maluski H., Rajlich P. and Matte P. (1993) ^{40}Ar–^{39}Ar dating of the Inner Carpathians Variscan basement and Alpine mylonitic overprinting. *Tectonophysics*, **223**, 313–337.

Marsina K., Bodiš D., Havrila M., Janák M., Káčer Š., Kohút M., Lexa J., Rapant S. and Vozárová A. (1999) *Geochemical Atlas of the Slovak Republic, part III: Rocks*. Pp 135, Ministry of Environment of the Slovak Republic, Geological Survey SR, Bratislava.

Mellini M. and Merlino S. (1977) Hellandite: a new type of silicoborate chain. *American Mineralogist*, **62**, 89–99.

Miyawaki R., Nakai I. and Nagashima K. (1984) A refinement of the crystal structure of gadolinite. *American Mineralogist*, **69**, 948–953.

Miyawaki R., Nakai I., Nagashima K., Okamoto A. and Isobe T. (1987) The first occurences of hingganite, hellandite and wodginite in Japan. *Journal of the Mineralogical Society of Japan* **18**, 17–30 [in Japanese with English abstract].

Miyawaki R., Momma K., Yokoyama K., Shigeoka M., Matsuraba S., Ito M., Nakai I and Kristiansen R. (2015) Mn-bearing hellandite-(Y) from the Heftetjern pegmatite, Tørdal, Norway. *The Canadian Mineralogist*, **53**, 345–356.

Montel J.M., Foret S., Veschambre M., Nicollet C. and Provost A. (1996) Electron microprobe dating of monazite. *Chemical Geology*, **131**, 37–53.

Mrose M.E. and Rose H.J. (1962) Behierite (Ta,Nb)BO_4, a new mineral from Manjaka, Madagascar. *Annual Meeting of the Geological Society of America*, 235 [abstract].

Oberti R., Ottolini L., Cámara F. and Della Ventura G. (1999) Crystal structure of non-metamict Th-rich hellandite-(Ce) from Latium (Italy) and crystal chemistry of the hellandite-group minerals. *American Mineralogist*, **84**, 913–921.

Oberti R., Della Ventura G., Ottolini L., Hawthorne F.C. and Bonazzi P. (2002) Re-definition, nomenclature and crystal-chemistry of the hellandite group. *American Mineralogist*, **87**, 745–752.

Oberti R., Langone A., Boiocchi M., Bernabè E. and Hawthorne F.C. (2019) News from the hellandite group: the redefinition of mottanaite and ciprianiite and the new mineral description of ferri-mottanaite-(Ce), the first Fe^{3+}-dominant hellandite. *European Journal of Mineralogy*, **31**, 799–806.

Oftendal I. (1964) On the occurrence and distribution of boron in pegmatite. *Norsk Geologisk Tidsskrift*, **44**, 217–225.

Ondrejka M., Uher P., Putiš M., Broska I., Bačík P., Konečný P. and Schmiedt I. (2012) Two stage breakdown of monazite by post-magmatic and metamorphic fluids: an example from the Veporic orthogneiss, Western Carpathians, Slovakia. *Lithos*, **142–143**, 245–255.

Ondrejka M., Putiš M., Uher P., Schmiedt I., Pukančík L. and Konečný P. (2016) Fluid-driven destabilization of REE-bearing accessory minerals in the granitic orthogneisses of North Veporic basement (Western Carpathians, Slovakia). *Mineralogy and Petrology*, **110**, 561–580.

Ondrejka M., Uher P., Putiš M., Kohút M., Broska I., Larionov A., Bojar A.-V. and Sobocký T. (2021) Permian A-type granites of the Western Carpathians and Transdanubian regions: products of the Pangea supercontinent breakup. *International Journal of Earth Sciences*, **110**, 2133–2155.

Pan Y., Fleet M.E. and Barnett R.L. (1994) Rare-metal mineralogy and geochemistry of the Mattagami lake volcanogenic massive sulfide deposit, Quebec. *The Canadian Mineralogist*, **32**, 133–147.

Panczer G., De Ligny D., Mendoza C., Gaft M., Seydoux-Guillaume A. and Wang X. (2012) Raman and fluorescence. Pp. 61–82 in: *Raman Spectroscopy Applied to Earth Sciences and Cultural Heritage* (J. Dubessy, M.-C. Caumon and F. Rul, editors). EMU Notes in Mineralogy **12**. European Mineralogical Union.

Parrish R.R. (1990) U-Pb dating of monazite and its application to geological problems. *Canadian Journal of Earth Sciences*, **27**, 1431–1450.

Pasero M., Kampf A.R., Ferraris C., Pekov I.V., Rakovan J. and White T.J. (2010) Nomenclature of the apatite supergroup minerals. *European Journal of Mineralogy*, **22**, 163–179.

Paulmann C., Zietlow P., McCammon C., Salje E.K.H. and Bismayer U. (2019) Annealing of metamict gadolinite-(Y): X-ray diffraction, Raman, IR, and Mössbauer spectroscopy. *Zeitschrift Für Kristallographie – Crystalline Materials*, **234**, 587–593.

Pautov L.A., Karpenko V.Yu. and Agakhanov A.A. (2013) Baratovite-katayamalite minerals from the Hodzha-Achkan alkaline massif (Kirgizia). *New Data on Minerals*, **48**, 12–36.

Pécskay Z., Lexa J., Szakacs A., Seghedi I., Balogh K., Konečný V., Zelenka T., Marinel K., Póka T., Fülöp A., Márton E., Panaiotu and Cvetković V. (2006) Geochronology of Neogene magmatism in the Carpathian arc and intra-Carpathian area. *Geologica Carpathica*, **57**, 511–530.

Perna M.G., Zaccaria D., Rosatelli G., Stoppani F.S., Curti E., Spratt J., Humphreys-Williams E., Najorka J., Brownscombe W., Nestola F. and Stoppa F. (2021) Dissolution-repackaging of hellandite-(Ce), mottanaite-(Ce)/ferri-mottanaite-(Ce). *Minerals*, **11**, 610.

Petrík I. and Konečný P. (2009) Metasomatic replacement of inherited metamorphic monazite in a biotite-garnet granite from the Nízke Tatry Mountains, Western Carpathians, Slovakia: Chemical dating and evidence for disequilibrium melting, *American Mineralogist*, **94**, 957–974.

Pieczka A., Hawthorne F.C., Cooper M.A., Szełęg E., Szuszkiewicz A., Turniak K., Nejbert K. and Ilnicki S. (2015) Pilawite-(Y), $Ca_2(Y,Yb)_2[Al_4(SiO_4)_4O_2(OH)_2]$, a new mineral from the Piława Górna granitic pegmatite, southwestern Poland: mineralogical data, crystal structure and association. *Mineralogical Magazine*, **79**, 1143–1157.

Plašienka D., Grecula P., Putiš M., Kováč M. and Hovorka D. (1997) Evolution and structure of the Western Carpathians: an overview. Pp 1–24i in: *Geological Evolution of the Western Carpathians* (P. Grecula, D. Hovorka and M. Putiš, editors). Mineralia Slovaca Monograph, Bratislava.

Plašienka D., Broska I., Kissová D. and Dunkl I. (2007) Zircon fission-track dating of granites from the Vepor-Gemer Belt (Western Carpathians): constraints for the Early Alpine exhumation history. *Journal of Geosciences*, **52**, 113–123.

Lo Pò D., Braga R., Massonne H.-J., Molli G., Montanini A. and Theye T. (2016) Fluid-induced breakdown of monazite in medium-grade metasedimentary rocks of the Pontremoli basement (Northern Apennines, Italy). *Journal of Metamorphic Geology*, **34**, 63–84.

Poitrasson F., Hanchar J.M. and Schaltegger U. (2002) The current state and future of accessory mineral research. *Chemical Geology*, **191**, 3–24.

Poller U., Janák M., Kohút M. and Todt W. (2000) Early Variscan magmatism in the Western Carpathians: U–Pb zircon data from granitoids and orthogneisses of the Tatra Mountains (Slovakia). *International Journal of Earth Sciences*, **89**, 336–349.

Pršek J., Ondrejka M., Bačík P., Budzyń and Uher P. (2010) Metamorphic-hydrothermal REE minerals in the Bacúch magnetite deposit, Western Carpathians, Slovakia: (Sr,S)-rich monazite-(Ce) and Nd-dominant hingganite. *The Canadian Mineralogist*, **48**, 81–94.

Putiš M. (1992) Variscan and Alpidic nappe structures of the Western Carpathian crystalline basement. *Geologica Carpathica*, **43**, 369–380.

Putiš M. (1994) South Tatric–Veporic basement geology: Variscan nappe structures; Alpine thick-skinned and extensional tectonics in the Western Carpathians (Eastern Low Tatra Mountains, Northwestern Slovak Ore Mountains). *Mitteilungen der Österreichischen Geographischen Gesellschaft*, **86**, 83–99.

Putiš M., Filová I., Korikovsky S.P., Kotov A.B. and Madarás J. (1997a) Layered metaigneous complex of the Veporic basement with features of the Variscan and Alpine thrust tectonics (the Western Carpathians). Pp 175–196 in: *Geological Evolution of the Western Carpathians* (P. Grecula, D. Hovorka and M. Putiš, editors). Mineralia Slovaca Monograph, Bratislava.

Putiš M., Unzog W., Wallbrecher E. and Fritz H. (1997b) Mylonitization and chemical mass-transfer in granitoid rocks of the Vepor pluton near the Cretaceous Pohorelá thrust (Veporic unit, central Western Carpathians). Pp 197–214 in: *Geological Evolution of the Western Carpathians* (P. Grecula, D. Hovorka and M. Putiš, editors). Mineralia Slovaca Monograph, Bratislava.

https://doi.org/10.1180/mgm.2022.7 Published online by Cambridge University Press

Putiš M., Kotov A.B., Petrík I., Korikovsky S.P., Madarás J., Salnikova E.B., Yakovleva S.Z., Berezhnaya N.G., Plotkina Y.V., Kovach V.P., Lupták B. and Majdán M. (2003) Early- vs. Late orogenic granitoids relationships in the Variscan basement of the Western Carpathians. *Geologica Carpathica*, **54**, 163–174.

Putiš M., Sergeev S Ondrejka M., Larionov A., Siman P., Spišiak J., Uher P. and Paderin I. (2008) Cambrian-Ordovician metaigneous rocks associated with Cadomian fragments in theWest-Carpathian basement dated by SHRIMP on zircons: a record from the Gondwana active margin setting. *Geologica Carpathica*, **59**, 3–18.

Putiš M., Ivan P., Kohút M., Spišiak J., Siman P., Radvanec M., Uher P., Sergeev S., Larionov A., Méres Š., Demko R. and Ondrejka M. (2009a) Metaigneous rocks of the West-Carpathian basement, Slovakia: indicators of Early Paleozoic extension and shortening events. *Bulletin de la Société Géologique de France*, **180**, 461–471.

Putiš M., Frank W., Plašienka D., Siman P., Sulák M., Biroň A. (2009b) Progradation of the Alpidic Central Western Carpathians orogenic wedge related to two subductions: constrained by 40Ar/39Ar ages of white micas. *Geodinamica Acta*, **22**, 31–56.

Pyle J.M., Spear F.S., Rudnick R.L. and McDonough W.F. (2001) Monazite–xenotime garnet equilibrium in metapelites and a new monazite–garnet thermometer. *Journal of Petrology*, **42**, 2083–2107.

Range K.-J., Wildenauer M. and Andratschke M. (1996) Crystal structure of tantalum orthoborate, $TaBO_4$. *Zeitschrift für Kristallographie*, **211**, 815.

Regis D., Cenki-Tok B., Darling J. and Engi M. (2012) Redistribution of REE, Y, Th and U at high pressure: Allanite-forming reactions in impure metaquartzites (Sesia Zone, Western Italian Alps). *American Mineralogist*, **97**, 315–328.

Reguir E.P., Chakhmouradian A.R. and Evdokimov M.D. (1999) The mineralogy of a unique baratovite- and miserite-bearing quartz – albite – aegirine rock from the Dara-i-Pioz complex, northern Tajikistan. *The Canadian Mineralogist*, **37**, 1369–1384.

Sauerer A. and Troll G. (1990) Abundance and distribution of boron in the Hauzenberg (Bavaria) granite complex. *Geochimica et Cosmochimica Acta*, **54**, 49–55.

Škoda R., Plášil J., Čopjaková R., Novák M., Jonsson E., Vašinová Galiová M. and Holtstam D. (2018) Gadolinite-(Nd), a new member of the gadolinite supergroup from Fe-REE deposits of Bastnäs-type, Sweden. *Mineralogical Magazine,* **82**, 133–145.

Spear F.S. and Pyle J.M. (2002) Apatite, monazite, and xenotime in metamorphic rocks. Pp 293–335 in: *Phosphates: Geochemical, Geobiological, and Materials Importance* (M.J. Kohn, J. Rakovan and J.M. Hughes, editors). Reviews in Mineralogy and Geochemistry, **48**. Mineralogical Society of America, Chantilly, Virginia, USA.

Thomas R. and Davidson P. (2017) Hingganite-(Y) from a small aplite vein in granodiorite from Oppach, Lusatian Mts., E-Germany. *Mineralogy and Petrology*, **111**, 821–826.

Tomašić N., Škoda R., Bermanec V. and Šoufek M. (2020) Crystal chemistry and microfeatures of gadolinite imprinted by pegmatite formation and alteration evolution. *American Mineralogist*, **105**, 1647–1655.

Uher P., Ondrejka M. and Konečný P. (2009) Magmatic and post-magmatic YREE- Th phosphate, silicate and Nb-Ta-Y-REE oxide minerals in A-type metagranite: an example from the Turčok massif, the Western Carpathians, Slovakia. *Mineralogical Magazine*, **73**, 1009–1025.

Uher P., Ondrejka M., Bačík P., Broska I. and Konečný P. (2015) Britholite, monazite, REE-carbonates and calcite: products of low-temperature alteration of allanite and apatite in A-type granite from Stupné, Western Carpathians, Slovakia, *Lithos*, **236–237**, 212–225.

Upadhyay D. and Pruseth K.L. (2012) Fluid-induced dissolution breakdown of monazite from Tso Morari complex, NW Himalayas: evidence for immobility of trace elements. *Contributions to Mineralogy and Petrology*, **164**, 303–316.

Vasyukova O.V. and Williams-Jones A.E. (2019) Closed system fluid-mineral-mediated trace element behaviour in peralkaline rare metal pegmatites: Evidence from Strange Lake. *Chemical Geology*, **505**, 86–99.

Villaseñor G., Catlos E.J., Broska I., Kohút M., Hraško L., Aguilera K., Etzel T.M., Kyle R.J. and Stockli D.F. (2021) Evidence for widespread mid-Permian magmatic activity related to rifting following the Variscan orogeny (Western Carpathians). *Lithos*, **390–391**, 106083.

Vojtko R., Králiková S., Jeřábek P., Schuster R., Danišík M., Fügenschuh B., Minár J. and Madarás J. (2016) Geochronological evidence for the Alpine tectono-thermal evolution of the Veporic Unit (Western Carpathians, Slovakia). *Tectonophysics*, **666**, 48–65.

Vozárová A., Rodionov N., Vozár J., Lepekhina E. and Šarinová K. (2016) U–Pb zircon ages from Permian volcanic rocks and tonalite of the Northern Veporicum (Western Carpathians). *Journal of Geosciences*, **61**, 221–237.

Wark D.A. and Miller C.F. (1993) Accessory mineral behavior during differentiation of a granite suite: monazite, xenotime, and zircon in the Sweetwater Wash pluton, southeastern California, USA. *Chemical Geology*, **110**, 49–67.

Warr L.N. (2021) IMA–CNMNC approved mineral symbols. *Mineralogical Magazine*, **85**, 291–320.

Williams M.L., Jercinovic M.J. and Hetherington C.J. (2007) Microprobe monazite geochronology: understanding geologic processes by integrating composition and chronology. *Annual Review of Earth and Planetary Sciences*, **35**, 137–175.

Williams M.L., Jercinovic M.J., Harlov D.E., Budzyń B. and Hetherington C.J. (2011) Resetting monazite ages during fluid-related alteration. *Chemical Geology*, **283**, 218–225.

Wing B.A., Ferry J.M. and Harrison T.M. (2003) Prograde destruction and formation of monazite and allanite during contact and regional metamorphism of pelites: petrology and geochronology. *Contributions to Mineralogy and Petrology*, **145**, 228–250.

https://doi.org/10.1180/mgm.2022.7 Published online by Cambridge University Press